

Tomographic Imaging Associated with a M_w 2.6 Fault-Slip Event in a Deep Nickel Mine

Ryan Joseph Molka

*Thesis submitted to the faculty of the Virginia Polytechnic Institute and State
University in partial fulfillment of the requirements for the degree of*

Master of Science
In
Mining Engineering

Erik C. Westman, Chair
Mario G. Karfakis
Kramer D. Luxbacher

04 May 2017
Blacksburg, VA

Keywords: passive tomography, induced tomography, mining, FMM, SIRT, stress

Tomographic Imaging Associated with a M_w

2.6 Fault-Slip Event in a Deep Nickel Mine

Ryan Joseph Molka

Abstract

Mine scale time-lapse passive tomographic imaging is a promising technique to monitor rock mass response brought on by mineral excavation. The ultimate goal of this study is to better understand rock mass response associated with rock failure so that we can forecast when rock failures may occur. Knowing this information can help engineers optimally design underground structures to avoid collapses that threaten miner safety, halt production, and close mines. This study utilized a tomographic inversion scheme that uses the Fast Marching Method (FMM) for raypath tracing and the Simultaneous Iterative Reconstruction Technique (SIRT) to solve the p-wave velocity model. The inversion scheme presented is tested using a data set from Creighton Mine in Sudbury, Ontario, Canada and includes 9,270 distinct events over 62 days. A total of 53 geophones recorded 191,856 p-waves that were used for inversion. Temporal monitoring of the seismic p-wave velocity in the vicinity of a known large M_w 2.6 fault-slip event was performed by calculating tomograms of the axial plane at the depth of the large event and of an oblique plane where there is a dense distribution of events. Tomograms were calculated on a weekly basis leading up to the event and also on a daily basis three days before the event. The tomograms reveal there are no trends in the models prior to the March 14th event to suggest that a large seismic event is about to occur. However, the datasets that include the seismic data from March 14th show a significant increase in p-wave velocity in the vicinity of the March 14th event location. The accuracy of the reconstructed velocity models were confirmed by using the checkerboard test with synthetic travel time data generated using the same event source and geophone location geometry as the original data. The checkerboard test confirmed the velocity models are accurate at voxels with two or more raypaths travelling through them. The consistent results observed and the good checkerboard correlation leads us to conclude that the inversion process presented in this paper is robust.

Tomographic Imaging Associated with a M_w 2.6 Fault-Slip Event in a Deep Nickel Mine

Ryan Joseph Molka

General Audience Abstract

One of the biggest challenges facing geoscientists is the ability to accurately predict failure within a rock mass. Conventionally, numerical modeling is performed to predict the response of the rock mass due to excavation. However, numerical modeling relies heavily on the estimated physical characteristics of the rock mass. Unless dense, costly sampling of the rock mass has been performed, the results of the modeling are not robust. Seismic tomography offers a unique advantage of monitoring the rock mass response over conventional numerical modeling because it is able to measure the true alteration in response to excavation (Westman, 2003). This paper utilizes a tomographic inversion scheme using the Fast Marching Method for raypath tracing and the Simultaneous Iterative Reconstruction Technique to solve the p-wave velocity model of an underground mine and surrounding rock mass. The inversion scheme presented is tested using a data set from Creighton Mine in Sudbury, Ontario, Canada and includes 9,270 distinct events over 62 days. A total of 53 geophones recorded 191,856 p-waves that are able to be used for inversion. Temporal monitoring of the seismic p-wave velocity in the vicinity of a known M_w 2.6 fault-slip event that occurred on March 14th is performed by creating tomograms of the axial plane at the depth of the event and of an oblique plane where a dense distribution of events occurred including the March 14th event. Tomograms are produced on a weekly basis leading up to the event and also on a daily basis three days before the event. The weekly tomograms reveal a decrease in p-wave velocity in the vicinity of the M_w 2.6 event as time approaches the event and then a significant increase 1,600 ft/sec larger than the background velocity the week of the event. The daily tomograms reveal a 1,200 ft/sec velocity increase in the same area from March 13th to March 14th, however, no trends in the daily or weekly tomograms prior to the date of the March 14th event suggest the known event is imminent.

Acknowledgements

First, I would like to thank my advisor, Dr. Erik Westman, for his continuous support throughout my collegiate career and for his guidance during this project. I consider myself very lucky to have had the opportunity to learn from such an influential member of the Virginia Tech community. I would also like to thank Dr. Mario Karfakis and Dr. Kray Luxbacher for agreeing to serve on my committee. I would like to thank the employees of Creighton Mine for collecting and supplying the seismic data used for this study and NIOSH for funding the research. I am grateful for the many influential friends I have made at Virginia Tech over the last six years and for their endless support. Finally, and most importantly, I would like to thank my family for believing undoubtedly in me and shaping me into the man I am today. None of my accomplishments would be possible without them.

Table of Contents

Table of Contents	iv
List of Figures	vi
List of Tables.....	vii
Chapter 1: Introduction	1
Chapter 2: Literature Review	3
2.1 - Seismology	3
2.1.1 – Earthquakes and Seismic Events	3
2.1.2 – Moment Magnitude Scale and Microseismicity	3
2.1.3 – Seismic Waves.....	4
2.2 – Rock Mechanics.....	6
2.2.1 – Microfracturing and Fracture Plane Development	9
2.2.2 – Rock Failures in Underground Mines	10
2.3– Tomography	11
2.3.1 – Principles of Travel-time Tomography	11
2.3.1.1 – Model Perturbation (Inversion).....	13
2.3.1.2 – Ray Tracing.....	13
2.3.1.3 – Common Tomography Schemes.....	14
2.3.1.4 – Model Confirmation.....	15
2.3.2 – Induced Seismicity as a Mechanism for Monitoring Underground Mines	16
2.3.2.1 – Challenges of Mining-Induced Passive Tomography.....	16
Chapter 3: Tomographic Imaging of Rock Mass Response Associated with a M_w 2.6 Fault-Slip Event in a Deep Nickel Mine	18
3.1 Abstract.....	18
3.2 Introduction.....	19
3.2.1 Site Description	20
3.2.2 Seismic Monitoring Equipment.....	21
3.2.3 Microseismic Data	22
3.3 Methods.....	25
3.3.1 Software Overview	25
3.3.2 Data Processing	27
3.3.3 Checkerboard Test Methods.....	28
3.3.4 Methods for Creighton Mine	28
3.4 Tomography Results and Discussion.....	30

3.4.1 Checkerboard Test Results	30
3.4.2 Tomography Iteration Results	31
3.4.3 Tomography Results.....	33
3.4.3.1 Weekly Tomography Results.....	33
3.4.3.2 Daily Tomography Results	37
Chapter 4: Summary of Results and Conclusions	41
4.1 Possible Sources of Error	42
4.2 Future Work	43
References	44
Appendix A: Determination of Node Spacing and Supporting Tomograms	47
Appendix B: Example SSR Curves.....	50
Appendix C: Weekly Tomograms.....	53
Appendix D: Blast Locations	55
Appendix E: Daily Tomograms	57

List of Figures

Figure 2.1: Nine Components of Stress	6
Figure 2.2: Mohr's Circle	7
Figure 2.3: Hypothetical Cracking Process	10
Figure 3.1: Cumulative daily event rate, summed daily.	23
Figure 3.2: Cumulative daily energy release, summed daily.....	23
Figure 3.3: Location of seismic events from Jan. 14 th to Mar. 14 th , 2009	24
Figure 3.4: Distance vs. time plot	25
Figure 3.5: Comparison of tomogram velocity isosurfaces at 19,700 ft/sec	28
Figure 3.6: Original checkerboard model vs. reconstructed checkerboard model at a depth of 7,600 ft	30
Figure 3.7: Iteration comparison for Jan. 25 th – Jan. 31 st dataset	32
Figure 3.8: Cross Sections on the axial plane at depth of March 14 th event taken from weekly tomograms.....	36
Figure 3.9: Daily difference tomograms	39
Figure A.1: Supporting tomograms for determining a grid size.....	49
Figure B.1: Example SSR vs. iteration number curves	52
Figure C.1: Cross Sections on the axial plane at depth of February 14 th event taken from weekly tomograms.....	54
Figure D.1: Weekly blasting locations.....	56
Figure E.1: Cross Sections on the axial plane at depth of March 14 th event taken from daily tomograms.....	58
Figure E.2: Cross Sections on Plane A coincidental to the March 14 th event taken from daily tomograms.....	60

List of Tables

Table 2.1: Physical properties of different materials	5
Table 3.1: Events and p-waves per weekly set	29
Table 3.2: Events and p-waves per daily set.....	29
Table 3.3: Optimum iteration per dataset	33
Table 3.4: Blasting frequency by week.....	37
Table A.1: Node spacing combinations	47

Chapter 1: Introduction

The biggest challenge facing geoscientists is the ability to accurately predict failure within a rock mass. Rock failure in an underground mine has the potential to threaten miner safety, halt production of ore, and close the mine. Conventionally, numerical modeling is performed to predict the response of the rock mass due to excavation. However, numerical modeling relies heavily on the estimated physical characteristics of the rock mass. Unless dense, costly sampling has been performed to characterize the rock mass, the results of the modeling are not robust. Seismic tomography offers a unique advantage of monitoring rock mass response over conventional numerical modeling because it is able to measure the true alteration in response to excavation (Westman, 2003). Tomography is a noninvasive method used to study the inside of a body. The information needed to conduct tomography is easily obtainable by seismic monitoring systems that may already be in place in many mines. Seismic tomography, as used in this thesis, is capable of imaging the p-wave velocity profile of an underground mine and surrounding rock mass which can be used to qualitatively infer where high stress zones are accumulating in the mine.

Little information is known about how a rock mass' properties change prior to and after naturally occurring earthquakes. Part of the problem of studying earthquakes is the inability to predict when and where an earthquake will occur. Naturally occurring earthquakes often do not produce enough seismic events for accurate tomographic application. Underground mines may be able to serve as "laboratories" for studying earthquakes because the act of mining induces seismicity at a rate sufficient for tomography to image the velocity profile of the surrounding rock mass. Mining induced tomography is also a useful tool for time-dependent studies since seismic data can be collected continuously. Time-lapse imaging of the three-dimensional p-wave velocity profile can be performed simply by dividing the data temporally and solving a tomogram for each set of data. Assuming that mining induced seismic events and naturally occurring earthquakes are caused by the same mechanisms, we may be able to study how a rock mass is responding prior to and after mining induced seismic events to make inferences about naturally occurring earthquakes.

This thesis will demonstrate the degree to which time-lapse tomography can be used to forecast a known large M_w 2.6 event by calculating p-wave velocity tomograms on a weekly and daily basis. The tomography code used in this study was written by Dr. Erik Westman. This

research is performed in order to build knowledge towards using tomography to forecast when large seismic events may occur in underground structures.

Chapter 2: Literature Review

2.1 - Seismology

2.1.1 – Earthquakes and Seismic Events

Earthquakes are violent releases of stored energy between two plates that shear past each other. The stored energy accumulates when frictional forces prevent relative movement between the plates and continues until the stored energy exceeds the friction and shearing occurs. When an earthquake occurs the energy is released primarily in the form of seismic energy, fracturing, and heat along the fault plane (Ma, 2014); however, it is well known that seismic energy, similar to that created by natural earthquakes, can be a response of human activity. Seismic energy in the form of seismic waves offer scientists on the surface a way to study the earth's complex interior.

Seismicity is defined as the temporal, spatial, and scalar distribution of earthquakes in a global or regional setting (Britannica, 2016). When seismic sources are intentionally created for the purpose of measuring seismic information, the practice is coined active seismicity. Active seismicity as an event source has several applications in modern exploration for collecting seismic data and exploring the subsurface. Some of the equipment and procedures used in industry for acquiring seismic data using active sources has been cataloged by Evans and includes vibrating machinery on the earth's surface, discharging explosives, weight dropping or thumper apparatuses, and marine air-guns to name a few (1997).

Passive seismicity implies that the source of seismic energy is a naturally occurring phenomena or is induced indirectly by another activity. Some examples of induced passive seismicity have been recorded by Guha and include seismicity following oil and gas extraction, seismicity induced by volcanic activity, and seismicity induced by underground mining (2000).

2.1.2 – Moment Magnitude Scale and Microseismicity

The most commonly accepted method for measuring the amount of energy released during an earthquake is the Moment Magnitude Scale developed by Hanks and Kanamori (1979). The Moment Magnitude Scale equation can be seen below:

$$M_W = \frac{2}{3} \log_{10}(M_0) - 10.7 \quad (1)$$

where $M_0 = \mu DA$ (N·m), is the seismic moment. D is the relative distance that one plate slides past the other, A is the area of the fault plane that sheared (both of which are inferred from seismograms) and μ is the rock rigidity. Due to the nature of the logarithmic equation, an increase of 1 on the moment magnitude scale corresponds to an approximate 32-times energy increase. Negative values of moment magnitude are also attainable which makes the equation suitable for quantifying smaller scale events such as those induced by mining. Microseismic events are defined by a moment magnitude of less than 0, which are too small of an energy release to feel on the surface.

2.1.3 – Seismic Waves

As mentioned previously, when a seismic event occurs one of the principle modes of energy release is in the form of seismic energy. There are two distinct types of seismic waves: surface and body waves. Surface waves consist of Raleigh waves and Love waves. These waves are much slower than the body waves. They move in a plane nearly parallel to Earth's surface and are often the cause of the most damage during earthquakes. The body waves consist of primary (p-waves) and secondary (s-waves) waves that can travel through the body of the earth. They are distinct from each other by the way they propagate through the ground. P-waves travel by the compression and rarefaction of a material in the direction of the wave. S-waves propagate by shearing the material transversely to the direction of travel. The velocity that p- and s-waves travel through a medium is given below,

$$v_p = \sqrt{\frac{k + \frac{4}{3}\mu}{\rho}} \quad (2)$$

$$v_s = \sqrt{\frac{\mu}{\rho}} \quad (3)$$

where k is the bulk modulus (incompressibility), μ is the shear modulus (rigidity), and ρ is the density of the medium the wave is traveling through. A closer inspection of Equation (3) suggests that the s-wave velocity reaches zero when the shear modulus is zero, as is the case for liquids. P-waves travel approximately 1.7 times faster than s-waves for many earth media. This

difference in speed is measured by seismograms to determine the epicenter of events. Table 2.1 lists the approximate laboratory p- and s-wave velocities through different media.

Table 2.1: Physical properties of different materials [after Bormann et al., 2012; *Suazo et al., 2017]

Material	Bulk Module (10 ⁹ Pa)	Shear Module (10 ⁹ Pa)	Density (kg m ⁻³)	Poisson Ratio	v _p (km s ⁻¹)	v _s (km s ⁻¹)
Air	0.0001	0	1	0.5	0.32	0
Water	2.2	0	1000	0.5	1.5	0
Diamond					18.0	
Sand & Sandstone	24	17	2500	0.21	4.3	2.6
Limestone	38	22	2700	0.19	4.7	2.9
Granite	56	34	2610	0.25	6.2	3.6
Basalt	71	38	2940	0.28	6.4	3.6
Cemented Paste Backfill*					1.1-3.5	

A raypath is the path that a seismic wave travels. Generally the raypaths of seismic events are not linear due to the heterogeneity of the rock mass it is traveling through. The degree of bending, θ_2 , associated with a raypath traveling from one medium to another can be expressed if both the index of refraction for both medias, n_1 and n_2 , and the angle of incident, θ_1 , are known by using Snell's Law:

$$n_1 \sin(\theta_1) = n_2 \sin(\theta_2) \quad (4)$$

While this expression for measuring the bending of raypaths is sound, applying it to trace the raypath of a seismic event is impossible due to the vast discontinuities that the raypath is likely to pass through from source to receiver.

In addition to raypath bending, the velocity of wave propagation through a medium can vary depending on the structure of the rock mass and its state of stress. Seismic waves can experience an increase or decrease in velocity due to varying stress conditions. The correlation between p-wave velocity and stress has been noted by Young and Maxwell (1992). An increase in velocity occurs during the initial loading of the rock specimen because it causes microcracks to close. As the load continues to increase, new microcracks are formed, decreasing the p-wave velocity. The ability to locate the origin of an event and infer the travel time from wave emission

to detection using a seismograph allows us to make inferences about the rock mass that the wave travelled through. The velocity at which an acoustic wave travels through a medium is a constant, physical property of the media. The average velocity of the seismic waves can be measured from the seismograph reading and the state of stress and integrity of the rock mass can be inferred.

2.2 – Rock Mechanics

Understanding stress distribution is critical in underground mine stability as an accumulation of stress can lead to ground failures such as rock bursts and roof falls. The safety of miners depends on our understanding of the local stress field. Stress is defined empirically as a force per unit area; however, stress also has an orientation. Moreover, a single point needs nine components to be fully characterized. These components can be seen below in Figure 2.1. Of these nine components, three are normal stresses that act perpendicular to a plane and the remaining six are shear stresses that act parallel to a plane.

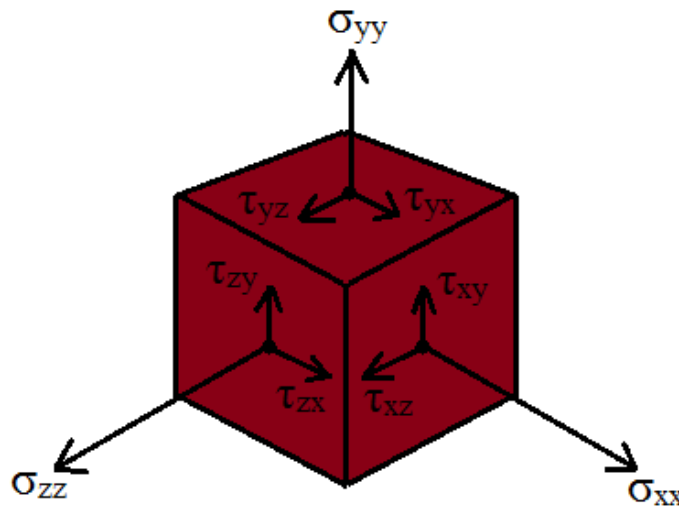


Figure 2.1: Nine Components of Stress to Define a Single Point

Failure of rocks occurs when the applied stress exceeds the ultimate strength of the rock. There are several different modes of rock failure which include (Goodman, 1989):

- *Flexure* – Failure associated with bending and propagation of tensile cracks. This mode of failure is often seen in the immediate roof of an underground mine.

- *Shear* – Failure where a plane is overcome with shear stress resulting in rock displacement. It is common in underground mines with weak roofs or floor.
- *Direct tension* – Common on slopes of high angles where a rock layer is displaced by its own weight.
- *Crushing* – Failure where particles and slivers between cracks cannot move and are crushed by the compression of the layer above them. Common among pillars in underground mines.

One of the most popular methods for determining the state of stress that will cause a rock to fail is the Mohr-Coulomb Failure Criterion. The Mohr's Circle, shown below in Figure 2.2, is used as a physical interpretation of the stress states that causes failure due to compression. Mohr's Circle also demonstrates that increasing the confining pressure increases the peak stress. One requirement for constructing Mohr's Circle is that the minor principal stress, σ_3 , must be greater than the uniaxial tensile strength of the rock. If it is not, this would imply tensile failure (Goodman, 1989).

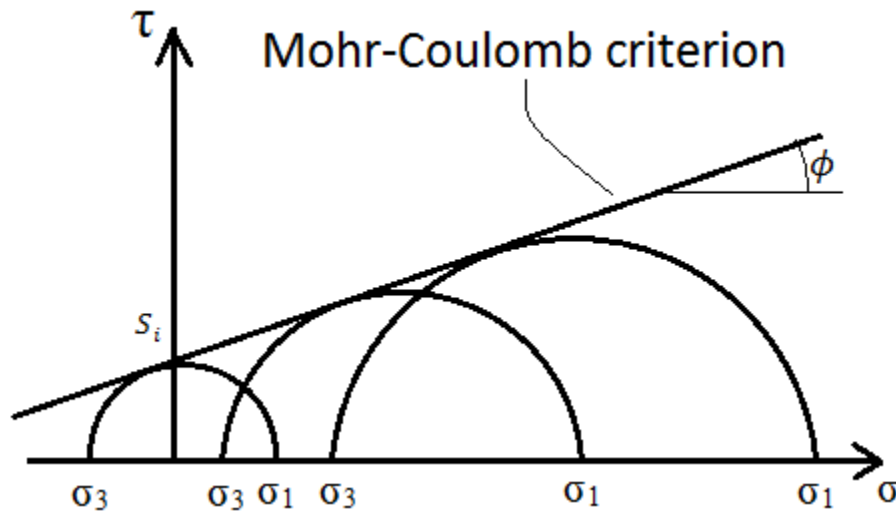


Figure 2.2: Mohr's Circle [after Goodman 1989]

The straight line tangent to the circles is the Mohr-Coulomb Failure Criterion and is given by:

$$\tau_p = S_i + \sigma \tan(\phi) \quad (5)$$

where

τ_p = shear strength on the plane of failure

S_i = cohesion

σ = normal stress on the plane of failure

ϕ = angle of internal friction

The angle ϕ of the line representing the Mohr-Coulomb Failure Criterion is related to the angle θ , the angle between the normal to the failure plane and the direction of major principal stress, by the following equation:

$$\theta = 45 + \frac{\phi}{2} \quad (6)$$

Another common failure criterion among mining engineers is the Hoek-Brown Failure Criterion. This method differs from the Mohr-Coulomb method because in many ways it is more applicable to a variation of rock species and accounts for some of their physical properties. For example, the Hoek-Brown Failure Criterion accounts for the Geological Strength Index, pore pressure, and near surface blast damage (Eberhardt, 2012). The Hoek-Brown Failure Criterion is not a linear relationship like the Mohr-Coulomb, it is parabolic in shape and given by the equation below (Eberhardt, 2012):

$$\sigma'_1 = \sigma'_3 + C_o \left(m_b \frac{\sigma'_3}{C_o} + s \right)^a \quad (7)$$

where

σ'_1 = major effective principal stress

σ'_3 = minor effective principal stress

C_o = uniaxial compressive strength

m_b, s, a = constants that depend on the Geological Strength Index (GSI), near surface blast damage (D), and a curve fitting parameter (m_i)

m_b , s , and a are given by the following set of equations provided by Hoek (2002):

$$m_b = m_i \exp\left(\frac{GSI - 100}{28 - 14D}\right) \quad (8)$$

$$s = \exp\left(\frac{GSI - 100}{9 - 3D}\right) \quad (9)$$

$$a = \frac{1}{2} + \frac{1}{6} \left(e^{-\frac{GSI}{15}} + e^{-\frac{20}{3}} \right) \quad (10)$$

These failure criteria are good laboratory estimations, but without supplementary stress measurement techniques the data is almost useless. Data needs to be collected from a mine and compared to the failure criterion to see if there is any risk of failures. Many invasive techniques currently exist to measure in-situ stresses; however, the problem with these techniques is that most of them require the region to be perturbed and can be labor intensive (Fairhurst, 2003).

2.2.1 – Microfracturing and Fracture Plane Development

According to Hoek, cracks can start to form well before the ultimate strength is reached, at about 40%-60% of the uniaxial compressive strength for low confined samples (2014). As mentioned earlier, as a rock undergoes stress, it experiences deformation. This deformation can account for the slippage and buckling of rock slivers between in situ cracks as well as the propagation of new cracks (Goodman, 1989). As more force is applied, these microcracks continue to propagate until the peak load is reached. Normally at this point, the microcracks join to create a fracture plane where shearing may occur. Figure 2.3 shows the hypothetical cracking process as the stress increases.

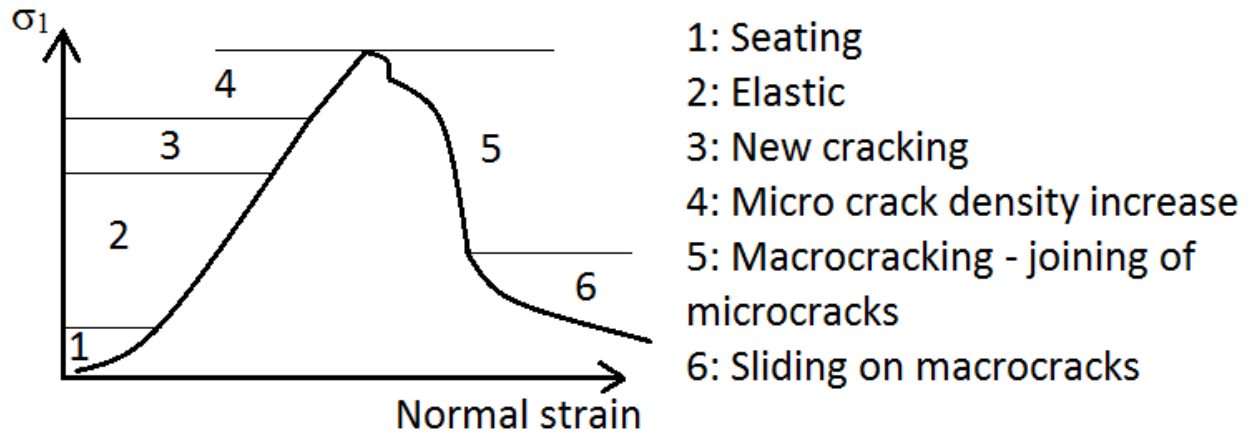


Figure 2.3: Hypothetical Cracking Process [after Goodman, 1989]

Several geological conditions contribute to the formation and growth of fractures. These include folding and faulting induced fracturing, naturally occurring hydraulic fracturing due to pore pressure, and lithology of the region (Liu, 2012). Fracturing can also be induced by mining operations as extension fractures are commonly seen within stope boundaries including the walls and advancing face (White, 1999) and in the roof near the corners of rectangular openings (White, 2004). These extension fractures can continue to develop and coalesce into a plane of weakness. Dilation can occur in these planes, or in bedding planes, in the direction of the mine opening due to stress relief. The weakening of the normal stress locking the two adjacent planes may be responsible for shearing on the fault plane. Other concerns resulting from fracturing around excavated areas include the sudden expulsion of rock into mined out areas also known as rock bursts and roof collapses (White, 2004). Rock bursts generally have a moment magnitude of 1.5 – 4.5.

2.2.2 – Rock Failures in Underground Mines

There are many modes of rock failures and the effects of any of them have the potential to be a threat to miner safety and economically costly. The source of mining induced microseismic events and deformation are often the result of stress redistributing underground within a rock mass in an attempt to reach a state of equilibrium. Stress redistribution is a result of excavation. As rock is excavated, the stress load carried by the excavated region is transferred to the surrounding rock mass; however, the transfer to the surrounding rock does not have to be uniform and can possibly relieve stress in certain areas and increase it in others. Predicting how

the rock mass will respond is difficult because of the complexity of the variables that play an effect. When investigating why a series of close proximity underground nickel mines in the Sudbury Basin have significantly different seismicity rates even though the geology and regional in situ stresses were similar, D.M. Morrison suggested that the difference could be because of significant lateral/vertical extent of mining with respect to host rock strength, structural complexity due to faults, proximity to mined out areas, and brittle enveloping strata (1993). Other parameters that are likely to affect seismicity are ore properties, country rock properties, strata geometry, local stresses, pore pressure, and extraction rate.

2.3– Tomography

Tomography is a method that is used to infer properties of a two- or three-dimensional body by measuring an energy source that has propagated through the body such as x-rays, first arrival times, full waveforms, etc. (Stewart, 1991). The purpose of tomography is to create a model of the desired property of the body. Tomography found its roots in the medical field as a way to study the inside of the human body noninvasively. After the success of computer axial tomography scanning in the medical industry in the 1970's, other industries such as geophysical exploration began to look for application. Keiiti Aki and William Lee are accredited for pioneering the work for utilizing seismic waves to create tomographic images of the subsurface (1976). Seismic tomography serves many purposes in the field of geoscience and exploration. Seismic monitoring can be held on a local or regional scale and has been used to model the velocity structure for a section of the San Andreas Fault (Aki & Lee, 1976), monitor a CO₂ plume during carbon sequestration (Slaker, 2011), and for inferring the stress redistribution around an underground coal longwall face (Luxbacher, 2008).

2.3.1 – Principles of Travel-time Tomography

There are several inversion techniques; the most common for seismic applications and the one used for this study is travel-time tomography. This process uses the travel times of first arrival p-waves emanating from a source to a sensor. Travel-time tomography is an iterative process in which the end product is a two- or three-dimensional velocity model of the volume that the rays propagated through. After the travel time data has been collected by geophones, a

three step process suggested by Emil Blias is performed (2005). First the theoretical travel-times are estimated by the use of an initial velocity model. The travel-times generated by the model are compared to the actual arrival times. If the times are not within an acceptable limit of error, the velocity model is perturbed to better fit the data. This process is iterated until the error is within acceptable limits. The resulting velocity model can then be used to create velocity tomograms.

Although the application of tomography to mining operations is somewhat recent, the mathematics behind the process has existed since the beginning of the 20th century with the revolutionary work of Johann Radon. In his 1917 paper, Radon mathematically proved the possibility of reconstructing a volume by using projection data that travelled through the volume (Radon, 1917). To reiterate this with respect to seismic travel-time tomography, Radon proved the possibility of reconstructing a volume of the subsurface p-wave velocity structure by using the travel times of p-waves that propagated through the structure. The travel time, t , of a ray propagating through a continuous velocity structure, $v(x)$ is:

$$t = \int_{L(v)} \frac{1}{v(x)} dl \quad (11)$$

where the raypath and the differential length along the path are denoted L and dl , respectively (Rawlinson & Sambridge). The $\frac{1}{v(x)}$ term, can be rewritten as the slowness of the structure $s(x)$.

A discrete form of Equation (11) can be written if the structure is discretized into M constant slowness blocks for N rays as follows:

$$\mathbf{d} = \mathbf{G}\mathbf{m} \quad (12)$$

where \mathbf{d} is the travel time residuals ($t_{\text{observed}} - t_{\text{calculated}}$) given by an $M \times 1$ vector, \mathbf{G} is a $N \times M$ matrix composed of ray lengths l_{ij} (the distance travelled by each ray in each block), and \mathbf{m} is the slowness perturbations given as an $M \times 1$ vector (Rawlinson & Sambridge). By solving for \mathbf{m} , it is possible to create a block model of the velocity structure which can be interpolated between the M nodes. This model can then be cut on any plane to further examine the changes in velocity around the structure. It is possible to monitor changes in stress in certain areas over time by performing this process with new data from the site. Ma confirmed the presence of stress

concentration in areas where major events occurred in an underground mine (2014). The ability to predict when and where rock bursts may occur because of stress accumulation over time is a valuable tool for mine operators in order to save lives.

2.3.1.1 – Model Perturbation (Inversion)

Tomography is commonly an iterative process where the model is perturbed so as to minimize the residual between the observed measurements and the calculated measurements obtained from the model. The modeled volume used in travel-time tomography is discretized into small cubes, also known as voxels. The voxels that are penetrated by raypaths are then perturbed using gradient methods, such as Gauss-Newton or subspace inversion, or by backprojection methods like the Algebraic Reconstruction Technique, ART, or the Simultaneous Iterative Reconstruction Technique, SIRT. The ART method is an iterative process where in a single iteration each raypath in the dataset is traced and the voxels along the raypath are changed to better reflect the travel time of the ray (Rawlinson & Sambridge, 2014). In a study in 1993 by Blundell, it is shown that ART is prone to converging poorly. SIRT functions similarly to ART, but instead of perturbing the voxels along raypaths and updating the velocity model for all raypaths one at a time, the perturbation applied to a voxel at the end of an iteration is the average perturbation from each raypath that travels through the voxel, thus, reducing the velocity anomalies brought on by poor convergence.

2.3.1.2 – Ray Tracing

Calculated travel times are computed using the source-receiver geometry in a velocity model of the subsurface. The raypaths of the seismic waves can be straight, but more realistic results are achievable if bent raypaths are assumed. SIRT requires accurate ray tracing. This can be accomplished using different methods such as shooting and bending, first arrival wavefront tracking, and Shortest Path Raytracing (Rawlinson & Sambridge, 2014). The Fast Marching Method, FMM, is a wavefront tracking method where the fastest travel time from source to receiver is determined using the current node velocities or slowness ($\text{slowness} = 1/\text{velocity}$) and can be used to trace bent rays (Sethian & Popovici, 1993). FMM works by starting at a point location, source location in the case of seismic ray tracing, and creating a band of trial nodes at the surrounding orthogonal nodes. The smallest slowness node of these trial nodes is considered

to be true and has its travel time correctly calculated. More trial nodes surrounding the true node are added to the trial band and the smallest slowness of these nodes is added to the true nodes. This process is repeated until the target node, receiver location for the raypath, is reached and turned true. Therefore, the path of the first arrival wave can be traced and travel time calculated (Rawlinson & Sambridge, 2014).

2.3.1.3 – Common Tomography Schemes

The inversion process of Aki and Lee uses a homogeneous velocity model to estimate the location of the events (1976). The inputs required to run the program include station coordinates, initial source parameters, observed first P-wave arrival times, and specifications for the initial crustal structure model. The program was tested by using artificial data from a known source and medium characteristics (Aki & Lee, 1976). The authors noted that the results showing the low velocity zone between the San Andreas and the Calaveras Faults are not definitive because of bias that may have been introduced by the simplified initial earth model. The authors propose that the errors can be reduced by implementing raypath tracing through heterogeneous models and collecting p-wave arrival times through denser arrays of geophones.

The program designed by Aki and Lee has been improved upon to increase the accuracy and resolution of the velocity model. This has been done through advancements in geophone spacing/positioning and programs that can trace bending raypaths. Improvements of the velocity resolution are accredited to using larger data sets thanks to greater computing power. Another method uses the full waveform equation to perform the inversion. Full waveform tomography inverts the amplitude and phase information of all arrivals. According to Gerhard Pratt, full waveform tomography offers greater resolution power than travel-time tomography because of the amount of information relevant in the wave equation (n.d.). However, the amount of information that needs to be processed requires significant computing power making it a much more expensive method.

Double difference tomography works under the assumption that if events are relatively close compared to the distance of a receiver, that the raypaths will share a nearly common path from event to receiver. Therefore, any difference in the travel times of the raypaths can be attributed to the spatial distance between the event locations. Waldhauser and Ellsworth used this

assumption to locate earthquake hypocenters by minimizing the difference between observed and calculated differential arrival times for two events (2000). The double difference equation is:

$$dr_k^{ij} = r_k^i - r_k^j = (T_k^i - T_k^j)^{obs} - (T_k^i - T_k^j)^{cal} \quad (13)$$

where $(T_k^i - T_k^j)^{obs}$ is the observed travel time differential between two events and $(T_k^i - T_k^j)^{cal}$ is the calculated travel time differential from a model. The double difference earthquake location algorithm is used in the tomography software *tomoDD* developed by Zhang and Thurber (2007 a). Their inversion scheme requires three types of data, the absolute arrival time, the differential arrival times, and the waveform cross-correlation, and works by simultaneously reconstructing the velocity model while locating seismic events. *TomoDD* has been shown to create sharp tomograms of the velocity model near event locations because of the inclusion of waveform cross-correlation data in the inversion process (Zhang & Thurber, 2007 a). The inversion process uses least squares regression analysis to determine which iteration has the model with the best fit for the data. A graph of the sum of squares vs. iteration number will often result in an L-shaped curve where the optimum iteration is at the “elbow” of the curve. While *tomoDD* is capable of producing quality tomograms, it can come with the price of heavy user manipulation in order to select the appropriate damping and smoothing parameters required for inversion (Zhang & Thurber, 2007 b).

2.3.1.4 – Model Confirmation

Model parameters used in seismic tomographic inversion are almost always unconstrained, meaning that there is no unique solution (Rawlinson & Sambridge, 2014). For example consider an inversion scheme utilizing SIRT, voxels outside the source-receiver geometry that have no rays traveling through them can take on any value and not change the results of the perturbation applied to the travelled through nodes. Observational errors can also account for model parameters in the solution to appear anomaly high or low in an attempt to fit the noisy data (Pei, n.d.). Therefore, solution parameters should be compared to the known parameters of the site to check the veracity of the solution.

Inversion robustness can be qualitatively examined by using a checkerboard resolution test. A checkerboard test is a synthetic test where the travel times are calculated through a known velocity structure using the same source-receiver geometry as the real data. The known velocity structure is an alternation of high and low velocity zones, appearing as a checkerboard. The principle idea is that after the synthetic travel times have been inverted using the questioned inversion scheme to create a model solution, areas that resemble the original checkerboard pattern are considered to be well resolved. The level of smearing may also be interpreted by examining the inverted checkerboard model. However, L  v  que et al. present evidence that the results of the checkerboard test may be misleading because it is possible that large scale structures could be poorly retrieved while small scale structures are well retrieved (1993). Synthetic data testing can still be used with several different synthetic models to understand the effect of different scaled structures on resolution.

2.3.2 – Induced Seismicity as a Mechanism for Monitoring Underground Mines

Microseismic tomography is a promising resource for monitoring the redistribution of stress around underground mines (Westman, 2004). The success of a tomographic study depends on the number and distribution of raypaths used for inversion. The number of raypaths depends on the number of sensors used in the array, the sensitivity of the equipment to detect microseismic events, and the number of seismic events. Studies utilizing mining induced seismicity generally accrue large data sets. Utilizing passive sources induced by mining activities for tomographic imaging offers several advantages to active sources including less labor intensive work, lower operational costs, and a noninvasive, continuous supply of data (Luxbacher, 2008).

2.3.2.1 – Challenges of Mining-Induced Passive Tomography

As previously mentioned, the distribution of raypaths plays a significant role in the reconstruction accuracy of the calculated velocity model. The model space should be encompassed with rays so the whole volume is well constrained. Areas of the model without sufficient raypath coverage will not have enough information to converge to the actual velocity of the area. The orientation of the rays should also vary so that the rays pass through the volume at various angles in order to avoid smearing of the reconstructed velocity model. This can be

achieved with a sensor array that encapsulates the entire volume (Westman, 2004). Elongation of a velocity anomaly, also known as smearing or striking, in a tomogram can occur when there is a large number of events relatively close to each other some distance away from sensors. The smearing will be oriented in the direction parallel to the dominant raypath direction.

Noisy data can also lead to inaccuracies in produced tomograms. Software that automatically picks the p- and s-wave arrival times from a seismograph can make mistakes if the background noise is of higher amplitude than the incoming p-waves. Complete masking of the p-waves is also possible and could cause s-waves to be misidentified as p-waves. Therefore, either incorrect p-wave travel times are calculated or s-waves that are picked as p-waves could be used in the inversion process and could skew the results. While it is theoretically possible to identify s-waves from p-waves by examining their velocities, due to the ratio of p-wave to s-wave velocity, we cannot say for sure if a ray is an s-wave or a slow p-wave travelling through backfill and mine workings without examining the waveform. Due to the time requirement of manually looking through thousands of waveforms, this is unfeasible. It is best to compare the results of inversion using sets of only p-waves to sets using the p-waves with the unidentifiable waves and using intuition and reasoning to determine which sets provide more realistic results.

Chapter 3: Tomographic Imaging of Rock Mass Response Associated with a M_w 2.6 Fault-Slip Event in a Deep Nickel Mine

3.1 Abstract

Mine scale time-lapse passive tomographic imaging is a promising technique to monitor rock mass response brought on by mineral excavation. The ultimate goal of this study is to better understand rock mass response associated with rock failure so that we can forecast when rock failures may occur. Knowing this information can help engineers optimally design underground structures to avoid collapses that threaten miner safety, halt production, and close mines. This study utilized a tomographic inversion scheme that uses the Fast Marching Method (FMM) for raypath tracing and the Simultaneous Iterative Reconstruction Technique (SIRT) to solve the p-wave velocity model. The inversion scheme presented is tested using a data set from Creighton Mine in Sudbury, Ontario, Canada and includes 9,270 distinct events over 62 days. A total of 53 geophones recorded 191,856 p-waves that were used for inversion. The mine volume was discretized to a 40x54x50 node model with node spacing of 83 feet in all directions. Temporal monitoring of the seismic p-wave velocity in the vicinity of a known large M_w 2.6 fault-slip event was performed by calculating tomograms of the axial plane at the depth of the large event and of an oblique plane where there is a dense distribution of events. Tomograms were calculated on a weekly basis leading up to the event and also on a daily basis three days before the event. The tomograms reveal there are no trends in the models prior to the March 14th event to suggest that a large seismic event is about to occur. However, the datasets that include the seismic data from March 14th show a significant increase in p-wave velocity in the vicinity of the March 14th event location. The accuracy of the reconstructed velocity models were confirmed by using the checkerboard test with synthetic travel time data generated using the same event source and geophone location geometry as the original data. The checkerboard test confirmed the velocity models are accurate at voxels with two or more raypaths travelling through them. The increase in the velocity model in the vicinity of the March 14th event from March 13th to March 14th is believed to be a response of two simultaneous ore production blasts that occurred on the morning of March 14th. It is likely that the blasts caused stress to be redistributed and accumulated towards the location of the M_w 2.6 event. The accumulated stress could have

exceeded the strength of the fault resulting in the increased event rate from 4 events/hour 1 hour before the blasts to a peak of 230 events/hour 16 hours after the blasts as well as the M_w 2.6 fault-slip event. The consistent results observed and the good checkerboard correlation leads us to conclude that the inversion process presented in this paper is robust.

3.2 Introduction

One of the biggest challenges facing geoscientists and engineers is the ability to accurately predict failure within a rock mass. Rock failure in an underground mine has the potential to threaten miner safety, halt production of ore, and close the mine. Conventionally, numerical modeling is performed to predict the response of the rock mass due to excavation. However, numerical modeling relies heavily on the estimated physical properties of the rock mass. Unless dense, costly sampling of the rock mass has been performed to find the real physical properties, the results of the modeling are not robust. Seismic tomography offers a unique advantage over conventional numerical modeling because it is able to measure the true alteration of the rock mass in response to excavation (Westman, 2003). Tomography is a noninvasive method used to study the inside of a body. Computer assisted tomography, or CAT scanning, is a well-known example of tomographic application in the medical field. CAT scanning utilizes x-ray projections through a body to create an image of the body's interior. Similarly, in the past 40 years, significant progress has been made in the geosciences to use seismic wave projections to image the interior of the Earth (e.g. Aki & Lee, 1976; Sethian & Popovici, 1993; Zhang & Thurber, 2007). More recently, there have been tomographic studies on the underground mine scale that utilize passive microseisms (small earthquakes) induced by mining as the source of seismic waves rather than active sources such as x-rays (e.g. Luxbacher et al., 2004; Ma & Westman, 2014).

Seismic tomography uses information contained in the seismic waveform that propagates from an event hypocenter to numerous geophones to calculate a model that can describe the information. In particular, the first arrival p-wave travel time data can be used to calculate a p-wave velocity model, or tomogram, that can explain the travel time data. The seismic events used in seismic tomography can be active sources or passive sources. Active sources imply that the source is purposely created in order to be recorded. Passive sources are created as a byproduct of another activity. In underground mines when excavation commences, the stress that was once

supported by the excavated volume is redistributed to the surrounding rock mass. The rock mass may then respond to this acquired stress by shifting in an attempt to reach a state of equilibrium which will create seismic events. According to Omori's law of temporal decay, seismic events can continue to occur for several days after the largest energy event occurs (Utsu, 1995). The advantages of using mining induced seismic sources over active sources is that it allows for continuous observation for time-dependent analyses and requires less personnel, lower operation costs, and is non-invasive (Slaker, 2011; Luxbacher, 2008).

A p-wave velocity model is sought after because it can qualitatively be related to the stress state of the rock mass (Young & Maxwell, 1992). The speed at which p-waves travel is dependent on the material they are traveling through. A highly fractured rock mass will have p-waves that travel slower than a fully competent rock mass of the same material due to the fractures. However, when the fractured rock mass is under stress, the fractures can close and the velocity of the p-wave will increase. Therefore, if tomograms of the p-wave velocity are created in temporal intervals, the relative change in velocity can be monitored and inferences of where highly stressed regions of the mine can be made. This information garnered from tomography can complement numerical modeling.

This thesis will demonstrate the degree to which time-lapse tomography can be used to forecast a known large M_w 2.6 event by calculating p-wave velocity tomograms on a weekly and daily basis. The tomography code used in this study was written by Dr. Erik Westman. This research is performed in order to build knowledge towards using tomography to forecast when large seismic events may occur in underground structures.

3.2.1 Site Description

Creighton Mine is located in Ontario, Canada and is one of the top ten deepest underground mines in the world. It has been a producer of nickel, copper, and several other metals for over 100 years. It is geologically located within the Sudbury Igneous Complex. The primary mining zone at Creighton Mine is characterized by a granite-gabbro footwall, a norite hanging wall, and a massive sulphide ore zone that composed of three subvertical joints and one low angle joint set. Core logging has been used to map the major and minor faults (Malik, 2008).

There are several different orebodies and different mining methods have been utilized depending on the structure of the orebody. The orebodies deeper than 6,400 feet in depth are

currently mined today using vertical retreat and slot-and-slash bulk mining. Slot-and-slash mining uses a top-down and center-out excavation sequence. The mined out area is then backfilled with cemented paste backfill that is created on site with the mill tailings (Malik, 2008).

Creighton has a long history of seismicity. Several large moment magnitude events have been recorded since the mine implemented a seismic monitoring system. The location of the seismic events has varied over time and with depth of mining. Shallow depth events occur mainly in crown pillars, intermediate depth events occur in the development heading, and deep events occur in sill accesses. Typically seismicity increases following production blasting in crown pillars. Statistical data collected by Creighton Mine has shown that most major events in the deepest parts of the mine have been caused by fault-slips (Malik, 2008).

3.2.2 Seismic Monitoring Equipment

Creighton Mine has a history of using microseismic monitoring systems since the 1980's. Currently there are two monitoring systems in place designed by Engineering Seismology Group. The first is a 104-channel ESG Hyperion system used to locate small seismic events and the second is a 24-bit ESG Paladin monitoring system that is primarily used to detect larger magnitude events. These systems have been used to observe seismic activity and predict potentially dangerous areas of the mine (ESG, n.d.).

This study used a total of 53 previously installed geophones to record seismic information. The geophones were installed in the active level of the mine and throughout the previous workings of the mine as shown in Figure 3.3 by the blue squares. The geophones provide sufficient three-dimensional coverage of the mine by fully encapsulating the workings. This ensures that the data set has a large quantity of p-waves that sample the interior of the mine and the immediately surrounding rock mass. The geophone array is not uniform in spacing and extends from -7,073 to -7,845 feet in depth, 4,384 to 5,891 feet in northing, and 3,242 to 4,453 feet in easting. The geophone array consisted of both uniaxial and triaxial sensors. Most of the sensors used have a frequency response of 100 Hz to 5,000 Hz; however, a small number have a low threshold of 50 Hz. The sensitivity of the geophones ranges from 0.3 to 980 V/g.

3.2.3 Microseismic Data

Microseismic data was provided for 62 days of continuous monitoring from January 14th to March 16th, 2009. The data includes coordinates for the event hypocenters and geophones that recorded the events, first arrival p-wave travel times, the amount of energy release, and other geophysical measurements of the events. The data was collected during normal operation of the mine. During the monitoring timespan, 30 production blasts were performed throughout various stopes. Three of the blasts were large crown blasts that involved approximately 5,500 to 14,520 lbs of explosives. The monitoring effort recorded 9,270 distinct seismic events. These events provided over 400,000 potential p-waves to be used in the tomography code. After processing data that did not have a travel time associated with it, there were 191,856 usable p-waves.

The hourly rate at which the seismic events occurred was not constant over time which was likely due to blasting. Figure 3.1 shows the daily event rate with respect to when blasting, crown blasting, and two noticeably large events occurred. Similarly, Figure 3.2 shows the amount of energy released daily with respect to the blast and large event dates. The figures show that spikes in event rates and energy release are preceded by blasts. This is especially noticeable on February 14th and March 14th; on these dates, the immediate largest events occur approximately 19 and 16.5 hours after the blasts. Swanson and Sines also identified an increase in seismicity following simultaneous blasting in different stopes in a lead-zinc-silver mine in the Coeur d'Alene mining district of northern Idaho, US (1991).

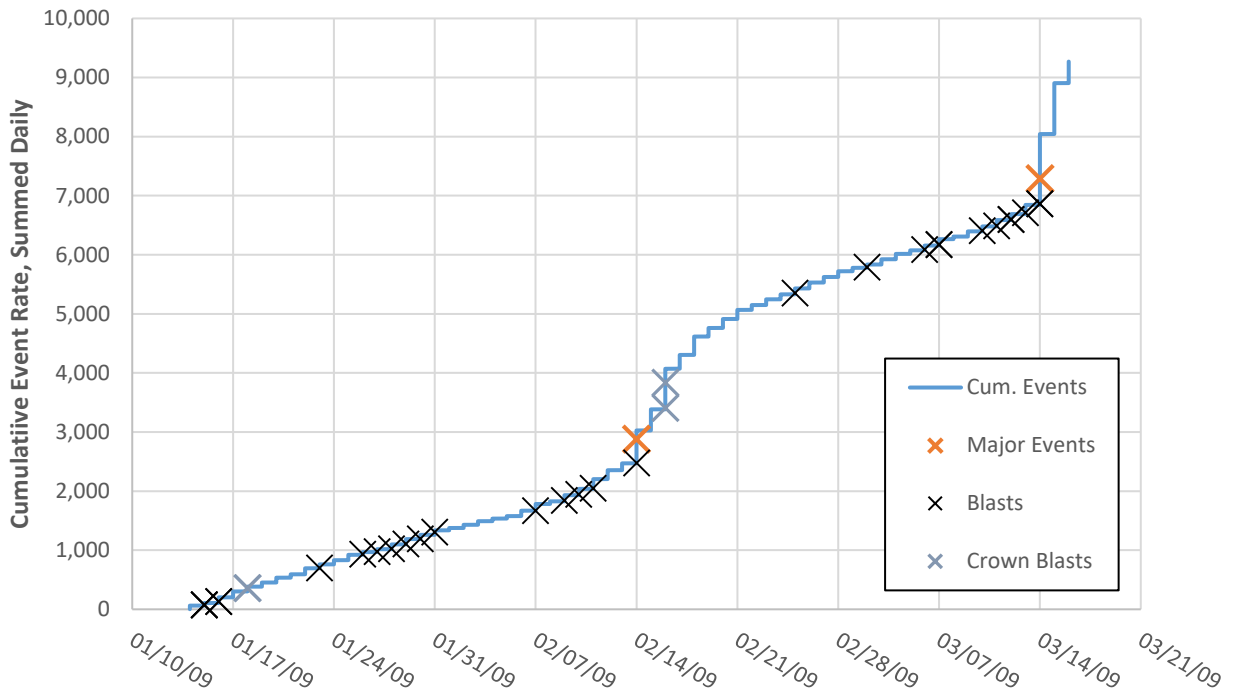


Figure 3.1: Cumulative daily event rate, summed daily.

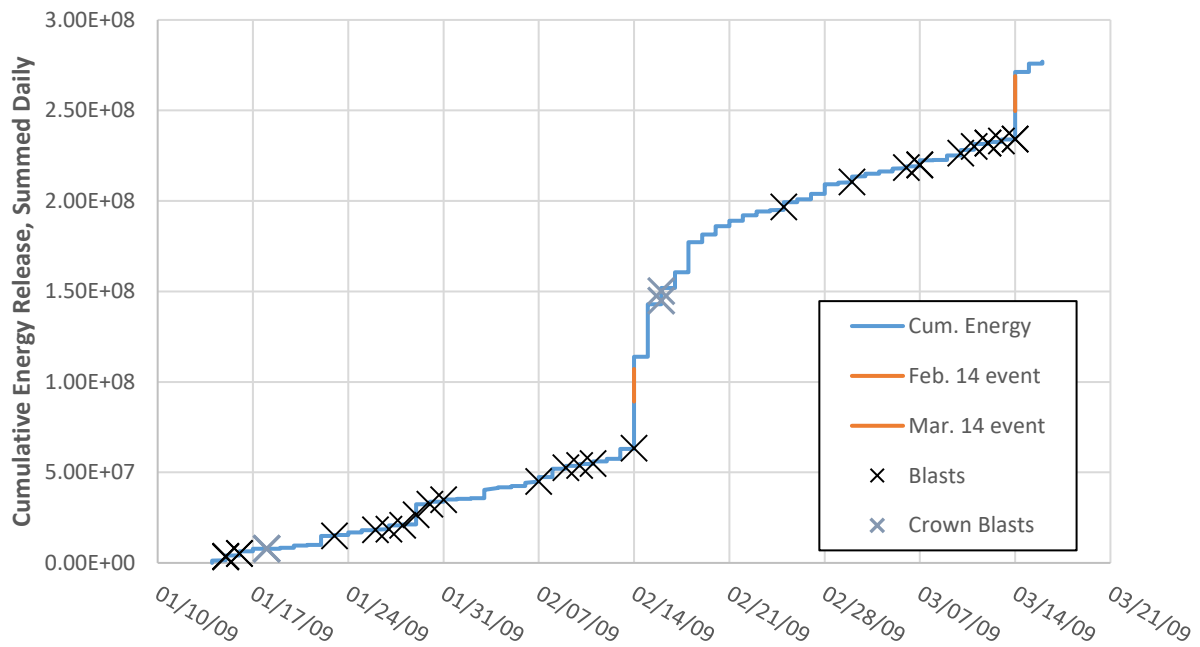


Figure 3.2: Cumulative daily energy release, summed daily.

Figure 3.3 shows the spatial distribution of the microseismic events. The left cluster of events in Figure 3.3 (b) contains 85% of the events. The dense cluster lays along a plane with an E-W strike at a dip of approximately 58 degrees. Geological data does not suggest that this is a fault, however, it remains an area of interest. Henceforth, this planar distribution of event will be addressed as “Plane A” throughout the rest of this thesis.

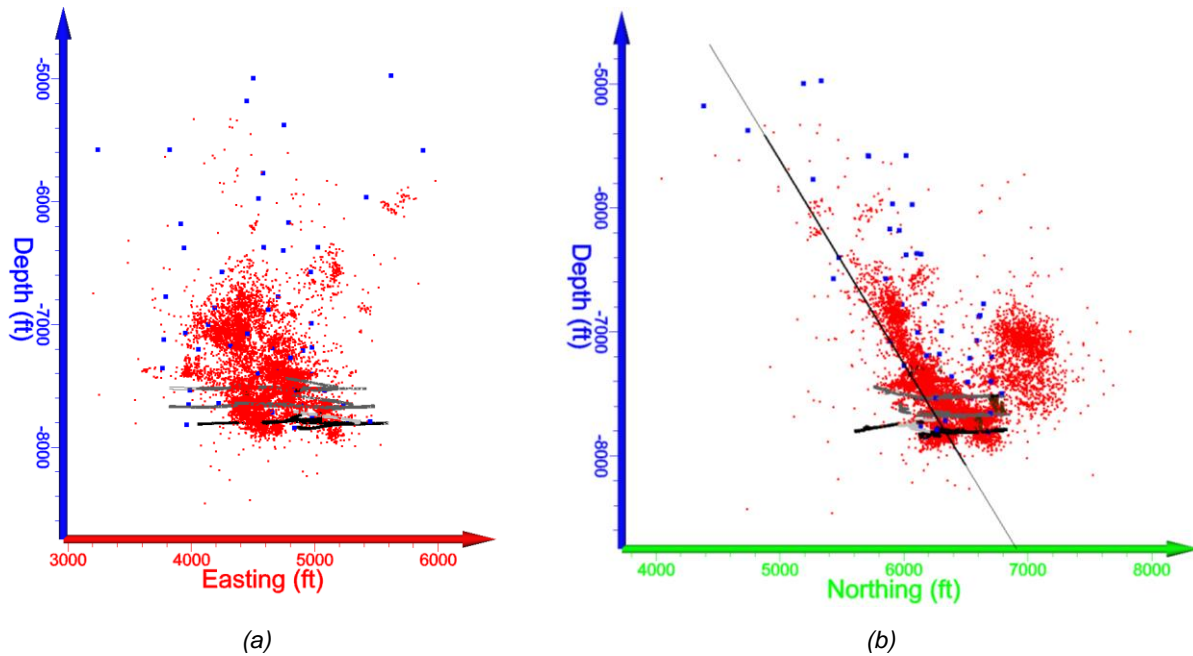


Figure 3.3: Location of seismic events (red circles) recorded from Jan. 14th to Mar. 14th, 2009 (a) Depth vs. Easting (b) Depth vs. Northing, cluster of dense distribution of events along Plane A is evident. Plane A is parallel to the distribution and coincides with the March 14th event. Geophones are represented by blue squares.

A plot of the distance travelled vs. p-wave travel time shown in Figure 3.4 shows there are two distinct velocities in the rock mass. The 20,000 ft/sec velocity is assumed to be the average background velocity of the rock mass since a majority of the events are along this line. There are two possible explanations for the slower 11,100 ft/sec velocity anomaly. First, the rays along this line may actually be s-waves that the monitoring system misidentified as p-waves. This is reasonable since the larger velocity is 1.8 times larger than the smaller velocity and p-waves are approximately 1.7 times faster than s-waves (Bormann et al., 2012). The second explanation is that the slower velocity is a result of the p-waves travelling through the backfilled stopes of the previously mined out areas. A study by Suazo et al. showed that the p-wave velocity through cemented paste backfill was in the range of 3,600 to 11,500 ft/sec (2017). The

effect that the uncertain rays have on the resultant tomograms was investigated and presented later in this thesis.

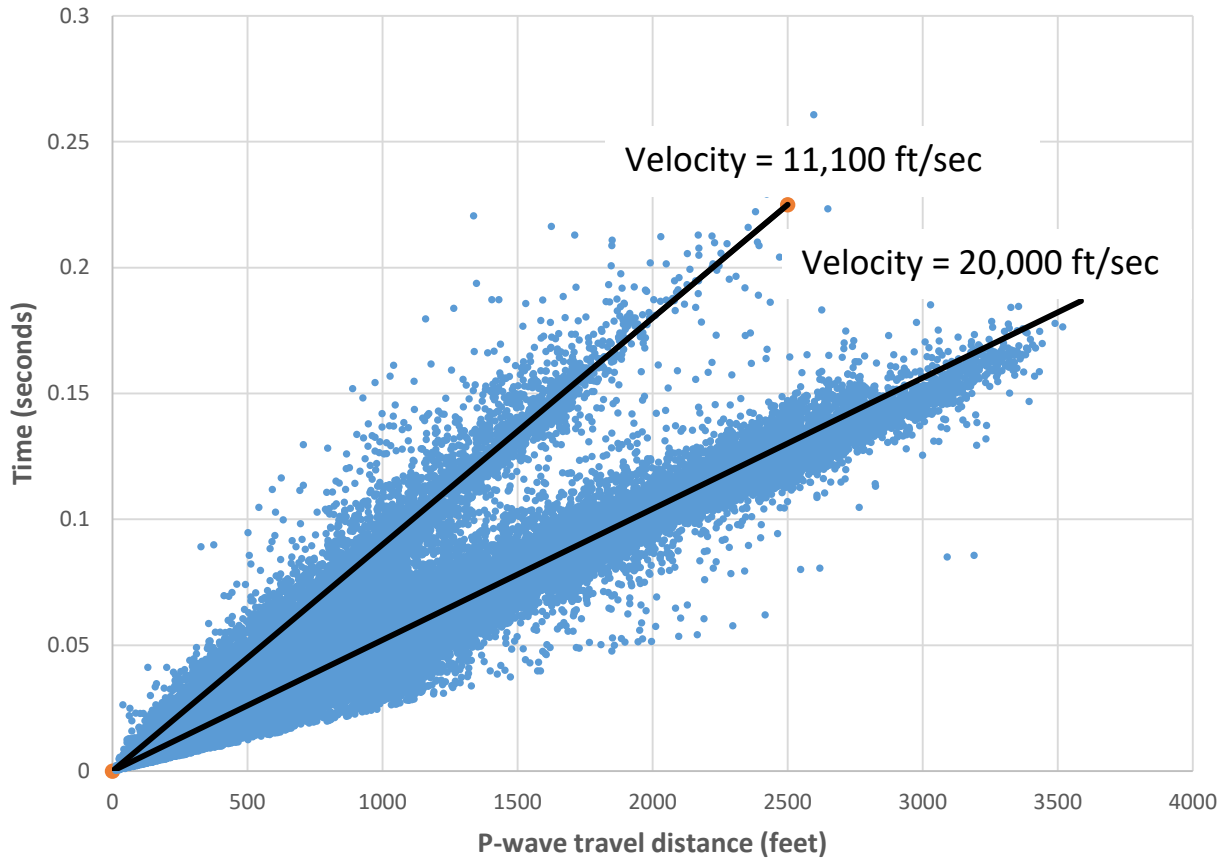


Figure 3.4: Distance vs. time plot for all rays recorded from Jan. 14th to Mar. 16th, 2009. The plot shows two distinct velocities attributed to the rock mass. The slower velocity may be misidentified s-waves or p-waves that travelled through cemented paste backfill. The faster velocity is believed to be the average background velocity.

3.3 Methods

3.3.1 Software Overview

In an effort to understand the alteration of the p-wave velocity field prior to a known large seismic event, the seismic data was split into weekly and daily sets to calculate time-lapse tomograms. Two MATLAB codes were written by Dr. Erik Westman for this study to calculate tomograms and confirm if the tomograms are accurate. A third program, Voxler 3, was used to visually render the two- and three-dimensional results.

The MATLAB code used to calculate the tomograms is not user intensive. A single input file containing the event hypocenter coordinates, geophone location coordinates, and first arrival p-wave travel time is needed for each ray that will be used for the inversion. Using this information, the spatial extents of the model are set to extend ten percent of the range in each direction. A fine grid spacing and a coarse grid spacing is determined by the user to discretize the velocity model into constant velocity blocks, or voxels. The spacing and number of voxels used will affect the resolution of the resultant velocity model. A model that is discretized too coarsely will result in a velocity model with poor resolution and will appear blocky. One that is discretized too finely will result in a model that has too much variation for the model to be geologically reasonable. The amount of voxels used will also have a significant effect on the computation time. The process used to select an appropriate grid spacing is discussed further in the Appendix A.

At the center of each voxel there is a node with a velocity value equal to the uniform velocity of the surrounding voxel. Each node within the velocity model is initially set to equal the background velocity of 20,000 ft/sec. A multistencil fast marching method code, `msfm3d.m`, is used to trace the propagation of the seismic wavefront orthogonally through the nodes of the velocity model (Kroon, 2009). This is done in order to find the path that the first arrival p-wave travelled from event hypocenter to geophone station and to calculate the approximate travel time of the p-wave. SIRT is then used to apply a velocity correction to each node of the model at the end of the iteration in order better fit the original travel time data as described by Rawlinson and Sambridge (2014). This process is repeated for multiple iterations until the residual between calculated travel times and original travel times are within an acceptable threshold or until the model converges.

A .txt file is generated at the end of each iteration with the coordinates and velocity value of all the nodes in the model. A program created by Golden Software, Voxler 3, is then used for visually representing the three-dimensional data. An inverse distance (power 1) interpolation method was used to produce a smooth image of the three-dimensional velocity model. Cross sections of the three-dimensional model were imaged at varying planes of interest for further investigation into the alteration of the velocity field prior to a large M_w 2.6 event.

The second MATLAB code written by Dr. Erik Westman performs a checkerboard test on the data set. In the checkerboard test, the user discretizes the model into a defined number of

nodes. A number of zones, or checkers, is defined by the user in each direction. The checkers themselves are composed of several nodes of constant velocity. The checkers are defined as high or low velocity in an alternating pattern resembling a checkerboard. Nodes within a high velocity checker are set to a user defined increase above the background velocity while nodes within a low velocity checker are decreased the same amount below the background velocity. Synthetic travel times are calculated from the original event-receiver pair locations using the multistencil fast marching method described previously. The synthetic travel times are then inverted using the tomography code in an attempt to recover the original, known checkerboard model. Sections of the reconstructed checkerboard model that are well resolved indicate sections of the volume that will produce good results for the original data.

3.3.2 Data Processing

As previously mentioned, the distance vs. time plot revealed that there are two distinct background velocities associated with the rock mass being studied. The low 11,100 ft/sec background velocity was explained to be either p-waves travelling through the cemented paste backfill or misidentified s-waves. Tomograms were calculated for the week of February 22nd to February 28th with and without the low velocity waves in an attempt to study the effect on the resulting tomogram. This was the only week this comparison was conducted due to time constraints. The tomogram that was calculated using the data set including the slow velocity waves showed significantly larger low velocity regions within the confines of the previously mined out areas. Figure 3.5 shows a comparison of the two tomogram's isosurfaces at a value of 19,700 ft/sec (1.5% below the 20,000 ft/sec background velocity). Since the isosurface increases in size almost entirely within the confines of the previously mined out areas, the slow 11,100 ft/sec velocity anomaly evident in Figure 3.4 is assumed to be slow p-waves travelling through cemented paste backfill and, hence, should be included in the inversion process.

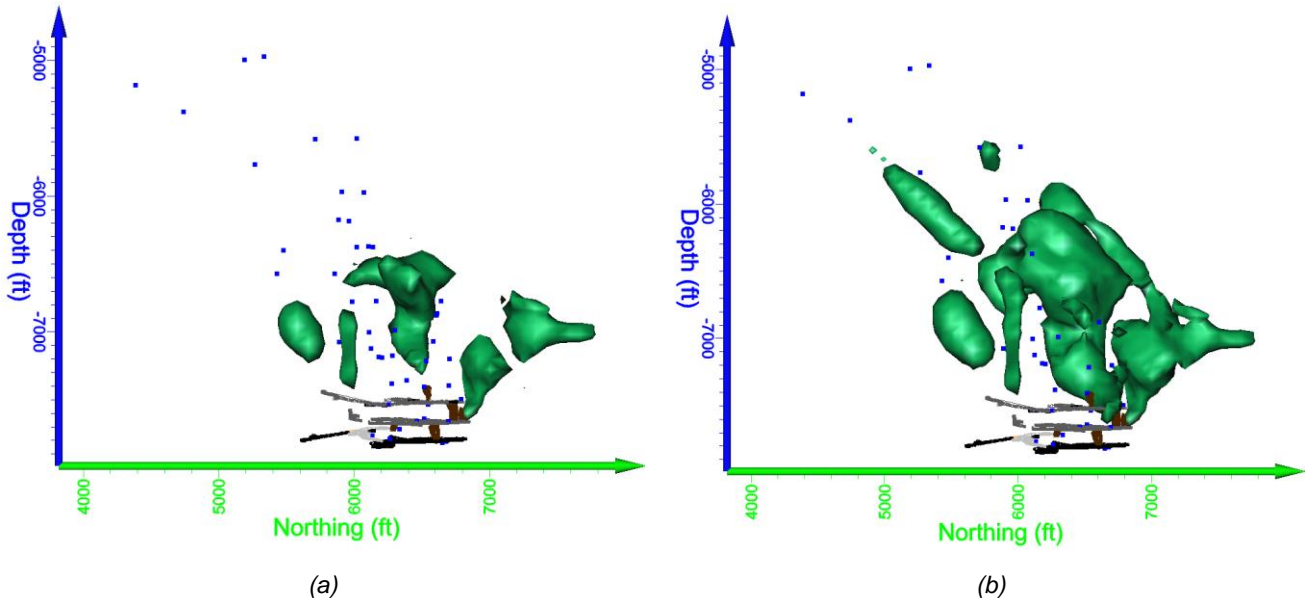


Figure 3.5: Comparison of tomogram velocity isosurfaces at 19,700 ft/sec (a) Tomogram calculated using high velocity p-waves (b) Tomogram calculated using high and low velocity p-waves. Test was performed to understand the effect of including the waves associated with the slow background velocity shown in Figure 3.4.

3.3.3 Checkerboard Test Methods

A checkerboard test was performed on the February 22nd to February 28th dataset to observe where the tomography code provides robust results for an average dataset. The model was discretized in the x, y, and z directions into a 160x240x200 voxel model. The checkers are composed of 20x20x20 nodes and have an alternating velocity of $\pm 10\%$ of the background velocity of 20,000 ft/sec. Further testing on other weekly sets was not performed due to time constraints.

3.3.4 Methods for Creighton Mine

A total of 9,270 events were recorded over 62 days of microseismic monitoring which provided 191,856 p-waves suitable for use in the tomography code after removing p-waves without a travel time associated with it. The p-wave data was split into weekly sets as shown below in Table 3.1. The data was split weekly rather than evenly amongst the number of raypaths because this is likely how mine operators would process data if the tomography code became a standalone product. The large number of events and raypaths from different orientations is sufficient for tomography, even for the smallest dataset.

Table 3.1: Events and p-waves per weekly set

Start Date	End Date	Number of Events	Number of Raypaths
Jan. 14	Jan. 24	831	13,604
Jan. 25	Jan. 31	505	8,512
Feb. 1	Feb. 7	446	9,255
Feb. 8	Feb. 14	1,245	27,121
Feb. 15	Feb. 21	2,040	41,282
Feb. 22	Feb. 28	654	13,755
Mar. 1	Mar. 7	543	11,774
Mar. 8	Mar. 16	3,005	66,553

The modelled volume was discretized into 40x54x50 voxels for each week of data. Each model started with an initial uniform velocity of 20,000 ft/sec. Weekly tomograms were created and cross sections of the tomograms were taken on the axial plane at the depth of the large February 14th event and the March 14th event.

The dataset was then split into weekly sets that overlap each other, but increment towards the March 14th event initially by two days, then by one day three days prior to the event as seen in Table 3.2. This was done to study how the velocity field was altering day-to-day. The tomography code was initialized using the same methods as the weekly tomography study.

Table 3.2: Events and p-waves per daily set

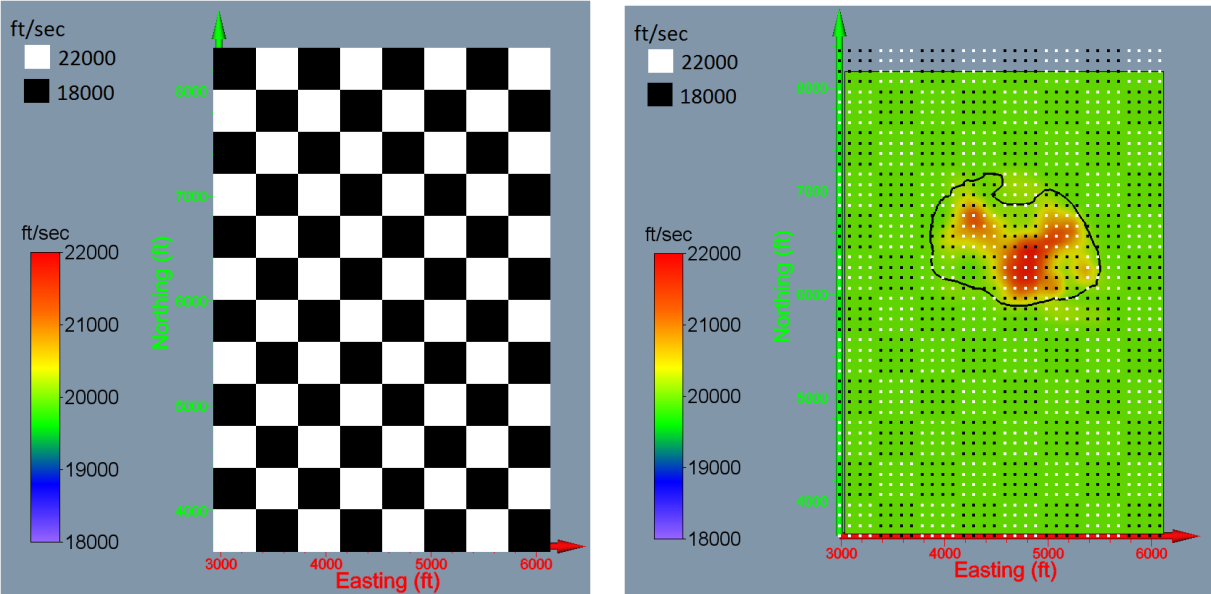
Start Date	End Date	Number of Events	Number of Raypaths
Mar. 1	Mar. 7	543	11,774
Mar. 3	Mar. 9	561	12,004
Mar. 5	Mar. 11	572	11,741
Mar. 6	Mar. 12	613	12,637
Mar. 7	Mar. 13	688	14,144
Mar. 8	Mar. 14	1,779	41,034
Mar. 9	Mar. 15	2,597	58,197

The tomograms calculated for the last four sets of data were each subtracted from the previous day's tomogram to emphasize where velocity was altering the most. Cross sections were produced on the axial plane at the depth of the March 14th event and on Plane A seen in Figure 3.3 (b). An inverse distance (power 1) interpolation method was used to calculate the velocity between the model's nodes. Any node with a velocity value that exceeded geologically reasonable explanation (100,000 ft/sec) was excluded from the interpolation so as to minimize its influence.

3.4 Tomography Results and Discussion

3.4.1 Checkerboard Test Results

Before the results of the weekly and daily tomography study are presented, the results of the checkerboard test are presented to understand where the tomograms are robust. Figure 3.6, shown below, shows the original checkerboard model and the reconstructed checkerboard model on the axial plane at a depth of approximately -7,500 feet. The cross section is in the middle of a row of checkers where the velocity is least affected by the surrounding opposite velocity checkers. The checkerboard test also revealed that voxels with two or more raypaths travelling through them are generally well resolved. A boundary of where voxels with exactly two raypaths traveling through them was drawn on all of the following tomograms to display where results are robust. It is also evident from the reconstructed checkerboard model, that there is little smearing of the velocity structure which indicates that the event-receiver geometry was capable of producing accurate results.



(a) (b)
Figure 3.6: Original checkerboard model vs. reconstructed checkerboard model at a depth of 7,600 ft (a) Original checkerboard model (b) Reconstructed checkerboard model at cross section in the center of a row of checkers. Black boundary is where voxels have two raypaths travelling through them. Inside of the boundary is considered to have robust results.

It is clear that the checkerboard model was reconstructed fairly well within the boundary where voxels have at least two raypaths travelling through them. The high velocity zones especially seem to reflect the original high velocity value of 22,000 ft/sec. However, the low velocity zones of the reconstructed velocity model appear to stay close to the initial velocity that the model was set to in the tomography code of 19,963 ft/sec rather than the 18,000 ft/sec low velocity zones in the checkerboard model. This is likely a consequence of when the synthetic travel times were calculated. The path that the multistencil fast marching method traces is likely to avoid the low velocity zones and travel predominantly through the high velocity zones in order to minimize the travel times. Therefore, there is likely little travel time data that samples the low velocity zones. Then during inversion, the initial values set in the low velocity zones are not altered much and stay approximately around 19,963 ft/sec. This explanation can confirm that the event-receiver geometry for the datasets is sufficient for tomographic analysis within the bounded region.

3.4.2 Tomography Iteration Results

It was mentioned previously in the Methods sections that a velocity model is calculated for each iteration of the tomography code. The model that best fits the data can be found by comparing the sum of squared residuals (SSR) value for each iteration. The SSR is a value that reflects how well the velocity model fits the original data. A decrease in SSR indicates an increase in the model fit. The equation used to find the SSR value for n p-waves for the j^{th} iteration is shown below:

$$SSR_j = \sum_{i=1}^n (i_{obs} - i_{calc})^2 \quad (14)$$

where i_{obs} is the original travel time and i_{calc} is the calculated travel time for the i^{th} p-wave.

Although generally after each iteration the SSR value decreases, the iteration that calculates the model of best fit is usually located at the “elbow” of the SSR vs. iteration number curve. Iterations after the elbow of the curve tend to “overfit” the model which can result in extremely large nodal velocity artifacts in the velocity model; however, the later iterations tend

to have little effect on overall “shape” of velocity profile, but rather effect the velocity quantitatively. This effect can be seen below in Figure 3.7.

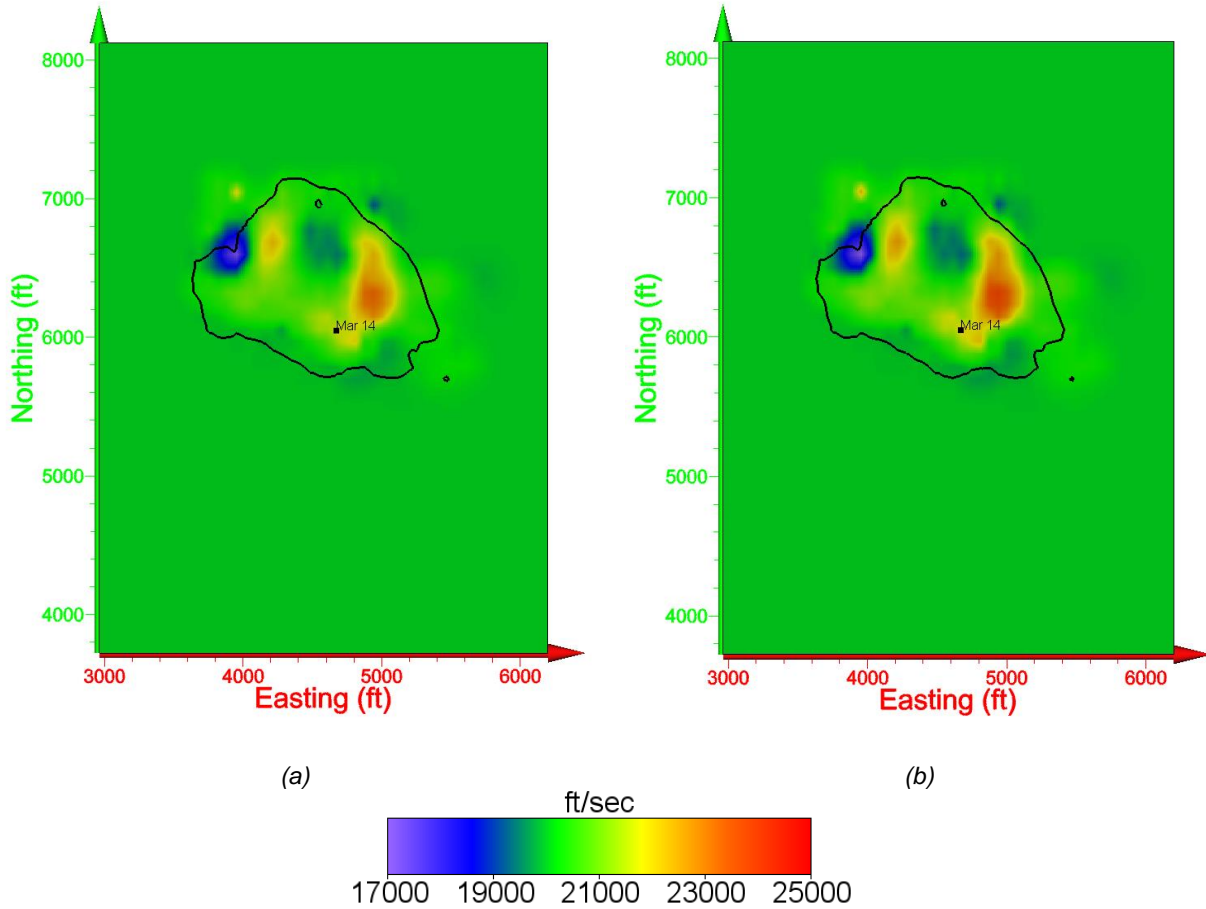


Figure 3.7: Iteration comparison for Jan. 25th – Jan. 31st dataset (a) iteration 9, optimum iteration (b) iteration 11, overfit iteration. The later iteration has the same shape as the previous iteration, but the velocity values are exaggerated.

An optimum iteration number at the elbow was picked by eye. The daily datasets all tended to have the same iteration number as the model of best fit. This was expected since the datasets share a lot of p-wave data. The weekly datasets did not share an iteration number that best fit the data. The iteration number that best fits each dataset is listed below in Table 3.3. Examples of the SSR vs. iteration number curves for some of the following tomograms are shown in Appendix B.

Table 3.3: Optimum iteration per dataset

	Start Date	End Date	Optimum Iteration Number
Weekly	Jan. 14	Jan. 24	10
	Jan. 25	Jan. 31	9
	Feb. 1	Feb. 7	8
	Feb. 8	Feb. 14	8
	Feb. 15	Feb. 21	7
	Feb. 22	Feb. 28	6
	Mar. 1	Mar. 7	6
	Mar. 8	Mar. 16	6
Daily	Mar. 1	Mar. 7	6
	Mar. 3	Mar. 9	6
	Mar. 5	Mar. 11	6
	Mar. 6	Mar. 12	6
	Mar. 7	Mar. 13	6
	Mar. 8	Mar. 14	6
	Mar. 9	Mar. 15	6

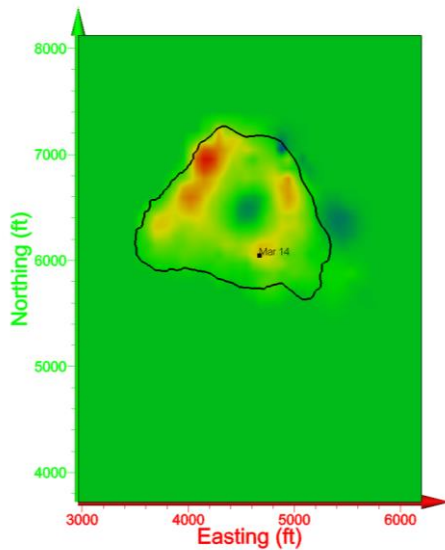
3.4.3 Tomography Results

3.4.3.1 Weekly Tomography Results

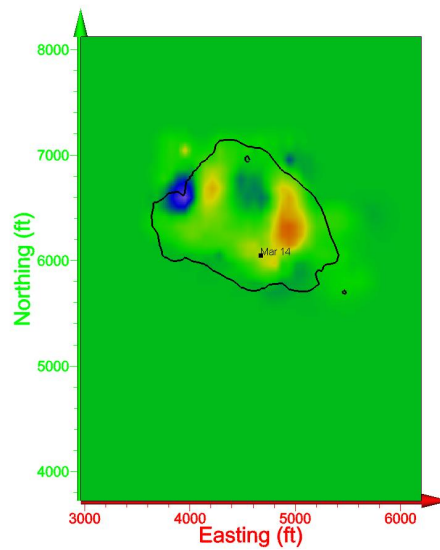
Cross sections on the axial plane at the depth of the February 14th and March 14th events were produced for each of the weekly time-lapse tomograms and are shown sequentially in Appendix C and Figure 3.8, respectively. Each of the cross sections in Appendix C and Figure 3.8 show a low velocity zone in the center of the model, Easting 4,600 feet, Northing 6,700 feet. The central low velocity zone is likely caused by the cemented paste backfill and previously mined out areas. This claim is supported by the consistency of the low velocity zone appearing in each of the weekly datasets and because the zone is within the premises of the previously mined out areas. All of the tomograms also have at least one low velocity zone laying approximately near the lateral extent of the mine. In particular, one zone appears in five of the eight tomograms. This low velocity zone lays east of the central low velocity zone. This zone may also be caused by the mined out areas, but the intermittency of the zone week-to-week may contradict this claim.

3.4.3.1.1 Weekly Velocity Trends in the Vicinity of High Energy Release Events

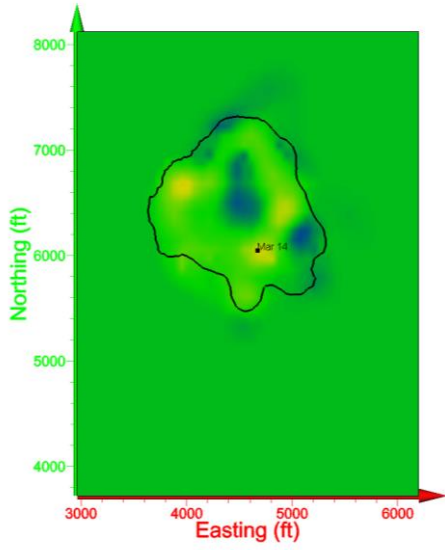
There are two large events that occurred during the monitoring period, but the results of the checkerboard test indicate that only the March 14th event has sufficient enough coverage to make interpretations. The February 14th event lies outside the boundary where voxels have at least two raypaths travelling through them for all the weekly sets except of the weeks of February 8th to February 14th and February 15th to February 21st. The cross sections reveal that the vicinity of the March 14th event experiences a range of different velocities week-to-week. The vicinity of the March 14th event location has a velocity of 2,000 ft/sec over the background velocity as early as January 24th as indicated in the January 14th to January 24th tomogram. The next six sequential cross sections show the velocity in the area of interest gradually recedes back to the background level of 20,000 ft/sec. The final weekly cross section, with the dataset that includes the March 14th M_w 2.6 event, shows a significant increase in the velocity in the vicinity of the event. The velocity exceeds the background velocity by 1,600 ft/sec.



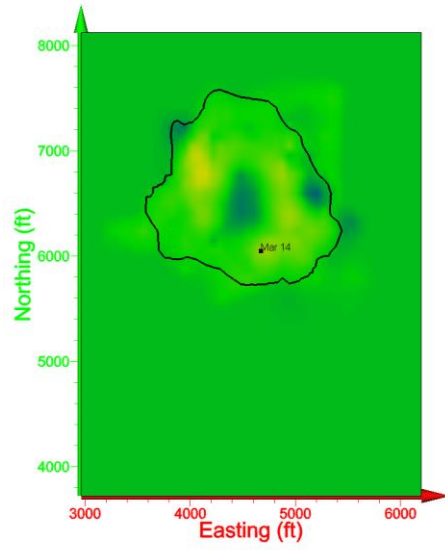
(a) Jan. 14th – Jan. 24th



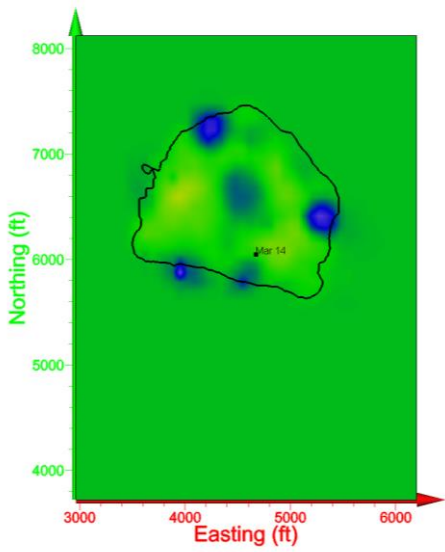
(b) Jan. 25th - Jan. 31st



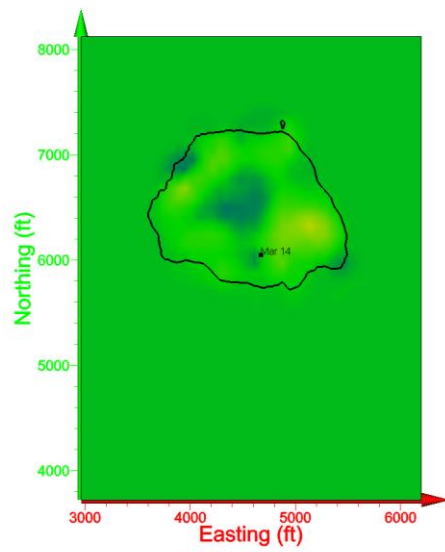
(c) Feb. 1st – Feb. 7th



(d) Feb. 8th – Feb. 14th



(e) Feb. 15th – Feb. 21st



(f) Feb. 22nd – Feb. 28th

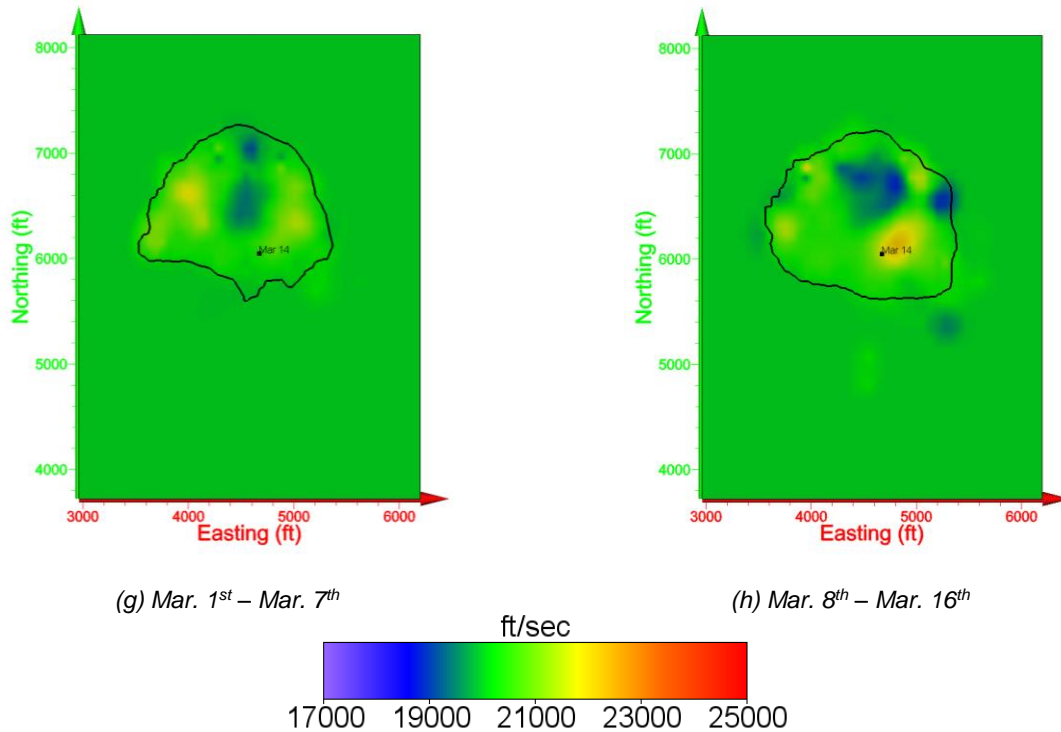


Figure 3.8:: Cross Sections on the axial plane at depth of March 14th event taken from weekly tomograms

The variation in velocity in the vicinity of the March 14th event location may be explained by the frequency of ore production blasting that occurred along, or very near Plane A. Table 3.4 describes the blasting schedule by week and indicates if there were any blasts during the week in a stope along Plane A. The locations of the weekly blasts in relation to the Plane A can be seen in Appendix D. The high velocity occurrence during the first week of data may be explained by the number of blasts that occurred that week in stopes that are along Plane A. It is possible that the blasting that occurred from January 14th to January 24th along Plane A redistributed the stress towards the vicinity of the March 14th event location. As a result of the frequency of blasting along Plane A decreasing during the next six weeks, the velocity in the vicinity of the March 14th event may have decreased gradually back to the normal background velocity. The velocity in the vicinity of the March 14th event location during the final weekly dataset may have increased significantly as a result of increased blasting along Plane A. It is possible that the blasts along Plane A may have redistributed stress towards the vicinity of the March 14th event which caused the accumulation in velocity and the large fault-slip event. The daily tomograms will provide more information about the velocity field leading up to the large event.

Table 3.4: Blasting frequency by week

Start Date	End Date	Number of Blasts	Number of Blasts on Plane A
Jan. 14	Jan. 24	5	3
Jan. 25	Jan. 31	6	1
Feb. 1	Feb. 7	1	1
Feb. 8	Feb. 14	4	1
Feb. 15	Feb. 21	2	1
Feb. 22	Feb. 28	1	1
Mar. 1	Mar. 7	4	1
Mar. 8	Mar. 16	7	4

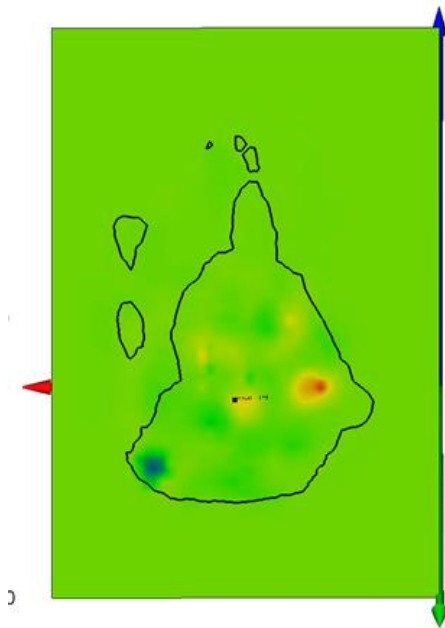
3.4.3.2 Daily Tomography Results

Cross sections of the axial plane at the depth of the March 14th event location were produced for each of the daily time-lapse tomograms calculated with the datasets described in Table 3.2. Additional tomograms were produced on Plane A, a plane of dense event distribution that the M_w 2.6 event occurred on. These cross sections are shown sequentially in Appendix E in Figures E.1 and E.2, respectively. The same low velocity zone that appears in the weekly tomograms was apparent in all seven of the daily tomograms. The first five cross sections of Figure E.1 are very consistent with one another with little variation and resemble the weekly cross section from March 1st to March 7th. The final two cross sections of Figure E.1 are also very consistent with one another and resemble the weekly cross section from March 8th to March 16th. This was anticipated since these datasets share a lot of the same data. As expected, the first five cross sections in Figure E.2 are very similar as are the final two cross sections in Figure E.2.

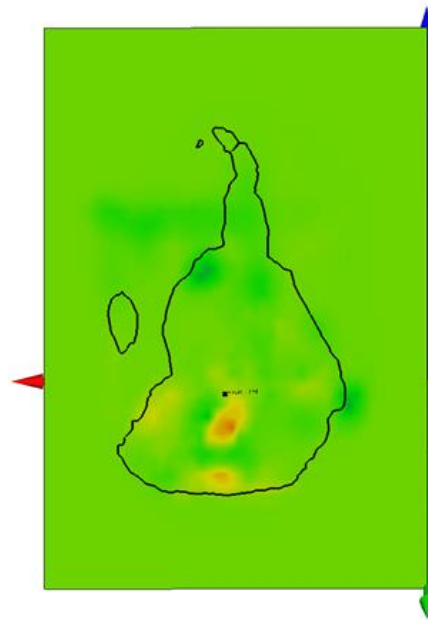
3.4.3.2.1 Daily Velocity Trends in the Vicinity of the March 14th Event Location

The cross sections produced on the axial plane shown in Figure E.1 and Figure E.2 show that there is little alteration to the velocity model in the vicinity of the March 14th event location until the dataset of March 8th to March 14th. This likely indicates that the mechanism responsible for the increase in velocity seen during the March 8th to March 14th tomogram did not occur until March 14th. This claim is further supported by the daily difference cross sections produced along Plane A (Figure 3.3 (b)) shown below in Figure 3.9. The daily difference cross sections show how much the velocity changed day-to-day for three days prior to the March 14th event. The

alteration in the vicinity of the March 14th event location from March 11th to March 12th is +250 ft/sec. The alteration from March 12th to March 13th, from March 13th to March 14th, and from March 14th to March 15th is +80 ft/sec, +800 ft/sec, and +50 ft/sec, respectively. The day that the high velocity zone receded back to the normal background velocity is unknown due to the dataset ending shortly after the event occurred.



(a) Mar. 11th to Mar. 12th



(b) Mar. 12th to Mar. 13th

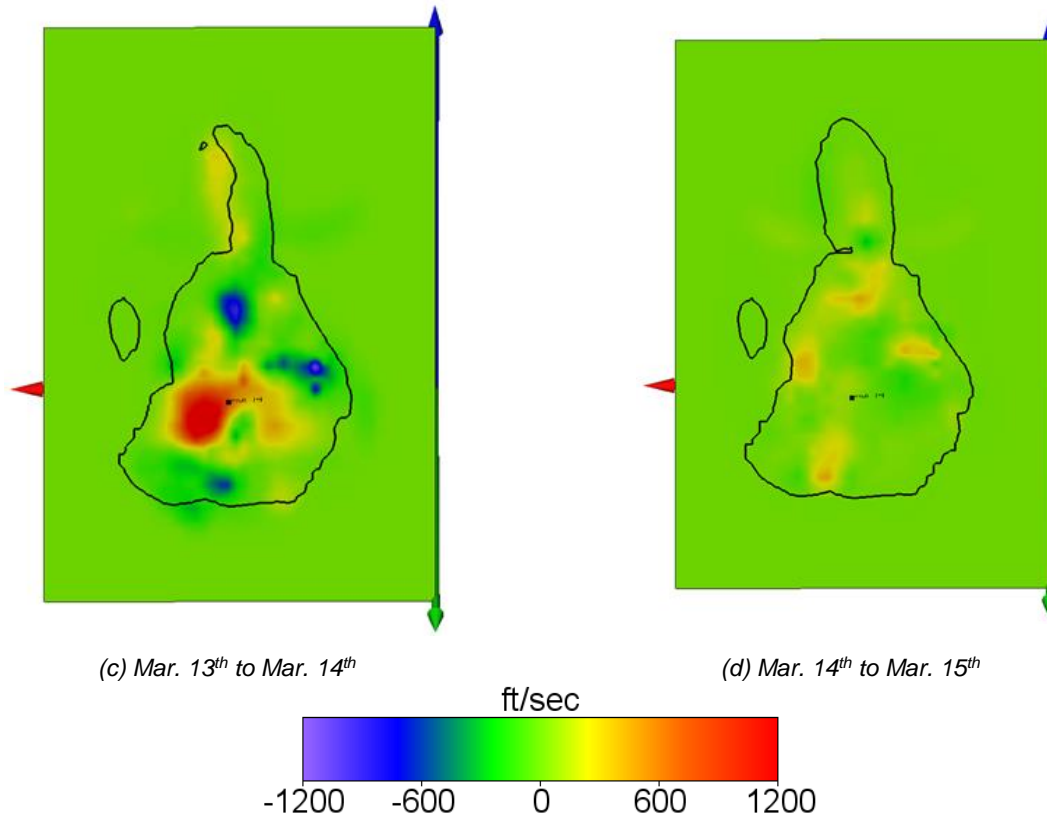


Figure 3.9: Daily difference tomograms

The only significant day-to-day change in velocity occurred from March 13th to March 14th and it is clear from Figure 3.9 (c) that a very large volume was affected. This is assumed to be a result of blasting that occurred at 2:08 AM on March 14th. There were two simultaneous blasts that occurred in two different stopes. One of the stopes is located on the Plane A and the other stope is approximately 500 feet north of the plane. It is likely that the two blasts redistributed stress that was once supported by the blasted volume towards the location of the March 14th event. This accumulation of stress explains why the p-wave velocity was anomalously higher in the vicinity of the event. It is likely that the rock mass was unstable and attempting to reach equilibrium, causing an increase in seismicity and the M_w 2.6 event. This claim is further supported by the increase in seismicity that was recorded immediately following the blasting. The hourly rate of seismicity increased from 4 events/hour 1 hour before the blasts to a peak of 230 events/hour 16 hours after the blasts.

Although the daily difference tomogram from March 13th to March 14th showed a significant increase in the velocity profile in the vicinity of the March 14th event location, the

daily tomograms failed to identify if the high velocity zone developed before or after the March 14th event and failed to identify a trend in the p-wave velocity that could be used to forecast the large M_w 2.6 event on March 14th. This indicates that the velocity significantly accumulated in a short span of time (less than a day). The rate that the velocity accumulated and when in relation to the event time it accumulated, were indeterminable using the weekly and daily datasets. Further investigation using a time-lapse of a few hours will be performed in the future to further investigate the potential of using tomography to forecast large seismic events in underground mines.

Chapter 4: Summary of Results and Conclusions

An underground nickel mine in the Sudbury Basin of Ontario, Canada was monitored for mining induced microseismicity from January 14th to March 16th. The p-wave data collected was used to calculate three-dimensional tomograms of the p-wave velocity for the mine and surrounding rock mass on a weekly basis leading up to a known M_w 2.6 event. Cross sections of the weekly tomograms were taken on the axial plane at the depth of a known M_w 2.6 fault-slip event that occurred at 6:27 PM on March 14 in an attempt to study the alteration of the p-wave velocity field leading up to the event. The cross sections show an approximate 2,000 ft/sec increase over the background p-wave in the vicinity around the location of the March 14th event as early as January 24th. The velocity in this vicinity gradually decreased over the next six weeks until significant blasting occurred in stopes along Plane A during the weekly dataset of March 8th to March 16th. The velocity model of March 8th to March 16th shows a significantly larger velocity around the event location than the previous week's models.

Daily tomograms were then calculated starting three days prior to the March 14th event to further study when the high velocity zone started to develop and to see if there was any trends in the velocity models to predict the large event on March 14th. Each daily tomogram was subtracted by the previous day's tomogram to show where the day-to-day changes to the velocity field were occurring. The only significant alteration in the vicinity of the M_w 2.6 event location occurred from the March 13th model to the March 14th model. The increase in the velocity in the vicinity was found to exceed 800 ft/sec. Although there is evidence that the velocity field alters in the same day as the large event on March 14th, no velocity trends in days prior to the event could be identified to forecast the event. The significant alteration of the velocity field from March 13th to March 14th, as indicated by the cross sections of the tomograms, may be related to the ore production blasting that occurred at 2:08 AM on March 14th.

Two production blasts were performed simultaneously in different stopes of the mine. One of the stopes lays closely along a plane where a dense distribution of events occurred, including the March 14th event. The other stope is approximately 500 feet north of this plane. It is likely that these blasts redistributed stress that was supported from the blasted section of the stopes to the high velocity zone that developed between the March 13th tomogram and the March 14th tomogram. This claim can be supported further by examining the seismicity rate around the time of the blasts. The event rate increased from 4 events/hr 1 hour before the blast to 230

events/hr 16 hours after the blasts. The significant increase in hourly event rate after blasting can be interpreted as the rock mass shifting in order to reach a state of equilibrium.

A checkerboard test using the same event-receiver pairs, but with synthetic p-wave travel times confirmed the inversion scheme could calculate accurate tomograms. In particular, the checkerboard test revealed that the tomograms were generally well-resolved for voxels that had more than two raypaths travelling through them. Although a significant increase in velocity was apparent in models that included the data from March 14th, this thesis failed to show that the weekly and daily tomograms were sufficient in forecasting the known large seismic event that occurred on March 14th. Additionally, the tomography code used in this study appears to be robust in its ability to measure the rock mass response due to mining based off the consistent tomograms that were calculated during both the weekly and daily tomograms, the good correlation results of the checkerboard test, and the identification of a high velocity zone during the day of the March 14th event.

4.1 Possible Sources of Error

There is a potential source of error in the methods used to pick the optimum iteration number for each dataset. Picking the optimum iteration number off the SSR vs. iteration number curve by eye can introduce bias. A mathematical approach to pick the optimum iteration number should be used so that any noticeable alteration in the velocity models is attributed to the changing conditions of the rock mass rather than an effect of choosing an inappropriate iteration number.

Another source of error in the resulting tomograms could be a result of how the seismic events are located. The ESG Hyperion and Paladin monitoring systems locate the hypocenters of seismic events using a uniform velocity model. Other tomography programs relocate the event hypocenters after the velocity models have been updated. Increased accuracy in the tomography code used to calculate tomograms in this study may be achievable if the hypocenters are relocated after each iteration of SIRT.

4.2 Future Work

Additional tomograms can be made on an hourly basis leading up to the M_w 2.6 event that occurred on March 14th in order to further study the rock mass behavior prior to and just after the time of the event. There is also the possibility of examining another large event that occurred on February 14th; however, the location of the event does not have sufficient raypath coverage which may result in the tomograms having poor resolution in the vicinity of the February 14th event. More studies on data sets from different mines is planned in an attempt to calculate tomograms that explain mine conditions that were documented by mine personnel. Studies will also be performed and resulting tomograms will be compared to numerical modeling results. Comparing the tomography results to documented mine conditions and numerical modeling results will further define the robustness of the tomography code.

Additionally, an algorithm to relocate seismic events after updating the velocity model each iteration may be tested to study its effect on the resulting tomograms. Future plans also include rewriting the tomography code in order to decrease computation time. This will likely be accomplished by introducing parallel processing.

The end goal of this research project is to create a mine monitoring system that can be used to monitor rock mass response and to forecast when large seismic events may occur in underground excavation projects. This information can be used as an engineering tool to help make more informed engineering decisions and thereby make deep underground mines safer.

References

- Aki, K., and W. H. K. Lee. "Determination of Three-Dimensional Velocity Anomalies Under A Seismic Array Using First P Arrival Times From Local Earthquakes 1. A Homogeneous Initial Model." *Journal of Geophysical Research* 81 (1976): 4381-399.
- Blias, E. "Seismic Traveltime Inversion." In *2005 Canadian Society of Exploration Geophysicists National Convention*
- Blundell, C. A. "Resolution analysis of seismic p-wave velocity estimates using reflection tomographic inversion." Diss. Monash University, 1993.
- Bormann, P., E. R. Engdahl, and R. Kind. "Seismic Wave Propagation and Earth Models." *New Manual of Seismological Observatory Practice 2*. Potsdam: GeoForschungZentrum, 2012. 9.
- Eberhardt, E. "ISRM Suggested Method: The Hoek-Brown Failure Criterion." *Rock Mechanics and Rock Engineering* 45 (2012): 981-88.
- Encyclopedia Britannica (2017). www.britannica.com, accessed Mar 1st, 2017.
- ESG. "Rockburst re-entry protocol at a deep underground Nickel mine in Sudbury, Ontario." N.d.
- Evans, Brian J. *A Handbook for Seismic Data Acquisition in Exploration*. Tulsa: Society of Exploration Geophysicists, 1997.
- Fairhurst, C. "Stress Estimation in Rock: A Brief History and Review." *International Journal of Rock Mechanics and Mining Sciences* 40 (2003): 957-74.
- Goodman, R. E. *Introduction to Rock Mechanics*. 2nd ed. New York: Wiley, 1989.
- Guha, S. K. *Induced Earthquakes*. Dordrecht: Kluwer Academic Publ., 2000.
- Hanks, T. C., and H. Kanamori. "A Moment Magnitude Scale." *Journal of Geophysical Research* 84 (1979): 2348-350.
- Hoek, E., and C. D. Martin. "Fracture Initiation and Propagation in Intact Rock - A Review." *Journal of Rock Mechanics and Geotechnical Engineering* 6 (2014): 287-300.
- Hoek E., C. T. Carranza-Torres, B. Corkum. "Hoek-Brown failure criterion-2002 edition." In *Proceedings of the fifth North American Rock Mechanics Symposium, Toronto, Canada* (2002): 267-73.
- J. Radon. "On the determination of functions from their integral values along certain manifolds." *Institute of Electrical and Electronics Engineers Transactions on Medical Imaging* 5 (1986): 170-76.

- Kroon, D. J. "Accurate Fast Marching." 2009.
<https://www.mathworks.com/matlabcentral/fileexchange/24531-accurate-fast-marching?focused=5175596&tab=function>
- Leveque, J. J., L. Rivera, and G. Wittlinger. "On the Use of the Checker-board Test to Assess the Resolution of Tomographic Inversions." *Geophysical Journal International* 115 (n.d.): 313-18.
- Liu, E., and A. Martinez. *Seismic Fracture Characterization: Concepts and Practical Applications*. Netherlands: EAGE, 2012.
- Luxbacher, K., E. Westman, and P. Swanson. "Time-Lapse Tomography of A Longwall Panel: A Comparison of Location Schemes." *Proceedings of the 26th International Conference on Ground Control in Mining*. West Virginia University, Morgantown (2008): 217-25.
- Ma, Xu, and Erik Westman. "Passive Seismic Tomography and Seismicity Hazard Analysis in Deep Underground Mines." Diss. Virginia Tech, 2014.
- Malik, F., C. Trifu, F. T. Suorineni, S. Espley, and M. Yao. "Management of High Stress and Seismicity at Vale Inco Creighton Mine." *American Rock Mechanics Association* (2008).
- Morrison, D. M. "Seismicity in the Sudbury Area Mines." *Proceedings of the 3rd International Symposium on Rockbursts and Seismicity in Mines*. Kingston, Ontario. Brookfield: A. A. Balkema, 1993. 379-82.
- Pei, D. "Three-dimensional Traveltime Tomography via LSQR with Regularization." *79th Annual International Meeting, Society of Exploration Geophysicists*. (n.d.): 4004-008. Print. Expanded Abstracts.
- Pratt, R. G. "Waveform Tomography: theory and practice." (n.d.).
- Rawlinson, N., A. Fichtner, M. Sambridge, and M. K. Young. "Seismic Tomography and the Assessment of Uncertainty." *Advanced Geophysics* 55 (2014): 1-76.
- Sethian, J. A., and A. M. Popovici. "3-D Traveltime Computation Using the Fast Marching Method." *Geophysics* 64 (1999): 516-23.
- Slaker, B., and E. Westman. "Double-Difference Tomography Applied to Monitoring of Geologic Carbon Sequestration in the Aneth Oil Field, Utah." Diss. Virginia Tech, 2011.
- Stewart, R. R. *Exploration Seismic Tomography Fundamentals*. Vol. 3. Tulsa, OK: Society of Exploration Geophysicists, 1991. Print. Course Notes Ser.
- Suazo, G., A. Fourie, and J. Doherty. "Experimental Investigation of Propagation and Transmission of Compressional Stress Waves in Cemented Paste Backfill." *Journal of Geotechnical and Geoenvironmental Engineering* 143 (2017).
- Swanson, P. L., and C. D. Sines. "Characteristics of Mining-induced Seismicity and Rock Bursting in a Deep Hard-rock Mine." Bureau of Mines Report of Investigation 9393 (1991).

- Utsu, T., Y. Ogata, and R.S. Matsu'ura. "The Centenary of the Omori Formual for a Decay Law of Aftershock Activity." *Journal of Physics of the Earth* 43 (1995): 1-33.
- Waldhauser, F., and W. L. Ellsworth. "A Double-difference Earthquake Location Algorithm: Method and Application to the Northern Hayward Fault, California." *Bulletin of the Seismological Society of America* 90 (2000): 1353-368.
- Westman, E. C. "Use of Tomography for Inference of Stress Redistribution in Rock." *Institute of Electrical and Electronics Engineers Transactions on Industry Applications* 40 (2004): 1413-1417.
- Westman, E. C., K. D. Luxbacher, and P.L. Swanson. "Local earthquake tomography for imaging mining-induced changes within the overburden above a longwall mine." *42nd U.S. Rock Mechanics Symposium, San Francisco, CA, The American Rock Mechanics Association* (2008).
- White, B. G. and J. K. Whyatt. "Role of fault slip on mechanisms of rock burst damage, Lucky Friday Mine, Idaho, USA." In *2nd Southern African Rock Engineering Symposium Implementing Rock Engineering Knowledge, Johannesburg, South Africa* (1999).
- White, B. G., M. K. Larson, S. R. Iverson. "Origin of mining-induced fractures through macroscale distortion." In *Proceedings of the Sixth North American Rock Mechanics Conference, Houston, TX, June5-10* (2004).
- Young, R. P., and S. C. Maxwell. "Seismic Characterization of a Highly Stressed Rock Mass Using Tomographic and Induced Seismicity." *Journal of Geophysical Research* 97 (1992): 12361-2373.
- Zhang, H., and C. H. Thurber. "Double-Difference Tomography: The Method and Its Application to the Hayward Fault, California." *Bulletin of the Seismological Society of America* 93 (2003): 1875-889.
- Zhang, H., and C. H. Thurber. "Estimating the Model Resolution Matrix for Large Seismic Tomography Problems Based on Lanczos Bidiagonalization with Partial Reorthogonalization." *Geophysical Journal International* 170 (2007): 337-45.

Appendix A: Determination of Node Spacing and Supporting Tomograms

The number of nodes to discretize the model into was determined by testing different fine and coarse node spacing combinations on the February 22nd to February 28th dataset. Other datasets were not tested due to time constraints. This data set was chosen because it has an average number of p-waves relative to the other data sets and the results for this set should hold for the other sets. The number of p-waves used in all the weekly sets can be seen in Table 3.1. The different node combinations that were tested on the February 22nd to February 28th data set as well as a qualitative description of the output velocity model can be seen below in Table A.1.

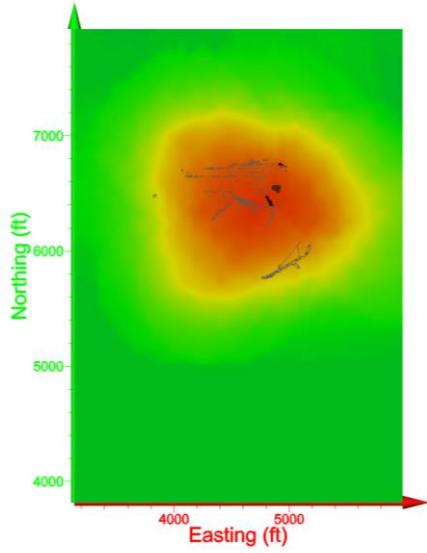
Table A.1: Node spacing combinations

# Coarse Nodes	# Fine Nodes	Quality of Resultant Tomogram
10	10	Poor
10	20	Poor
20	20	Fair
20	40	Poor
40	40	Good

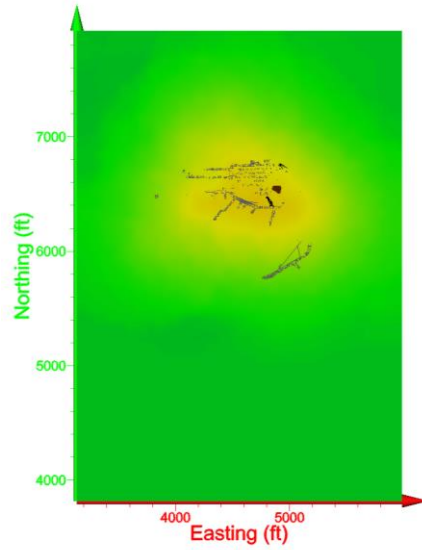
The node combination that is considered the most geologically reasonable was determined when evaluating the location of various isosurfaces. An isosurface is a three-dimensional surface of constant p-wave velocity. Geologically reasonable models generally show low velocity through the mined out areas and slightly higher velocity outside the perimeter of backfilled stopes. The node combination using a minimum of 40 coarse nodes and 40 fine nodes had the most geologically reasonable results indicating that the minimum number of nodes in a single direction should be approximately 40 for our datasets. Since the spatial extents of the data in the x, y, and z directions varied, the model was discretized into a 40x54x50 voxel model with node spacing equal to 83 feet for each of the tomograms that will be shown throughout this thesis. An axial cross section of each resulting tomogram was produced at a depth of -7,500 feet and can be seen in Appendix A.

Appendix A includes cross sections of tomograms that were created using different combinations of coarse and fine node spacing. This was done to find a grid spacing that could most accurately produce geologically reasonable tomograms. The cross sections were produced

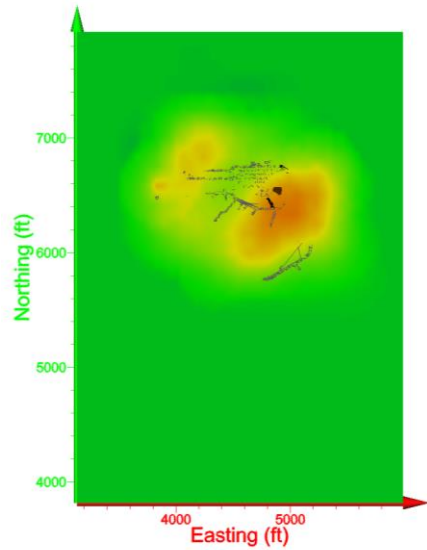
on the axial plane at a depth of -7,500 feet. The previous workings of the mine are displayed in the cross sections to help determine if the results of the tomogram make geologic sense.



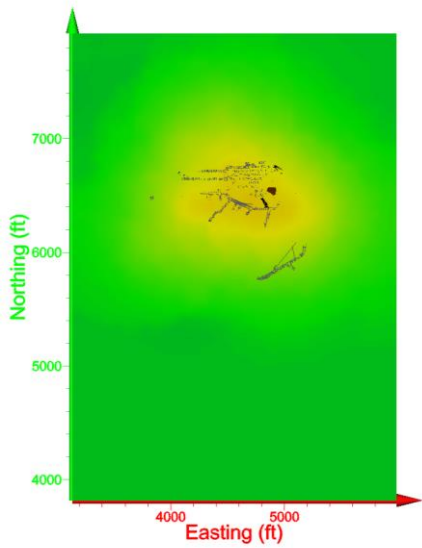
(a) Coarse 10, Fine 10



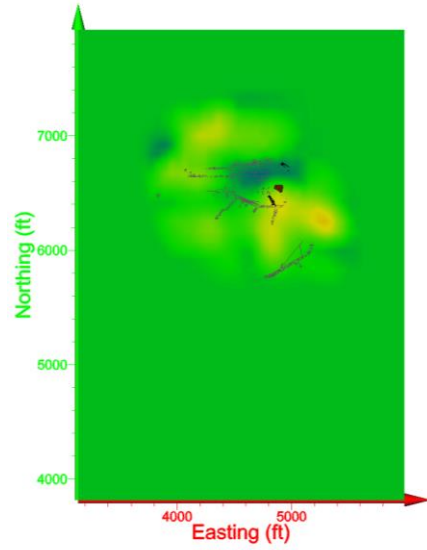
(b) Coarse 10, Fine 20



(c) Coarse 20, Fine 20



(d) Coarse 20, Fine 40



(e) Coarse 40, Fine 40
ft/sec

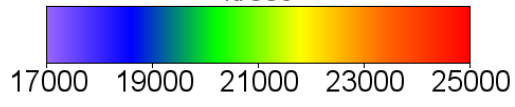
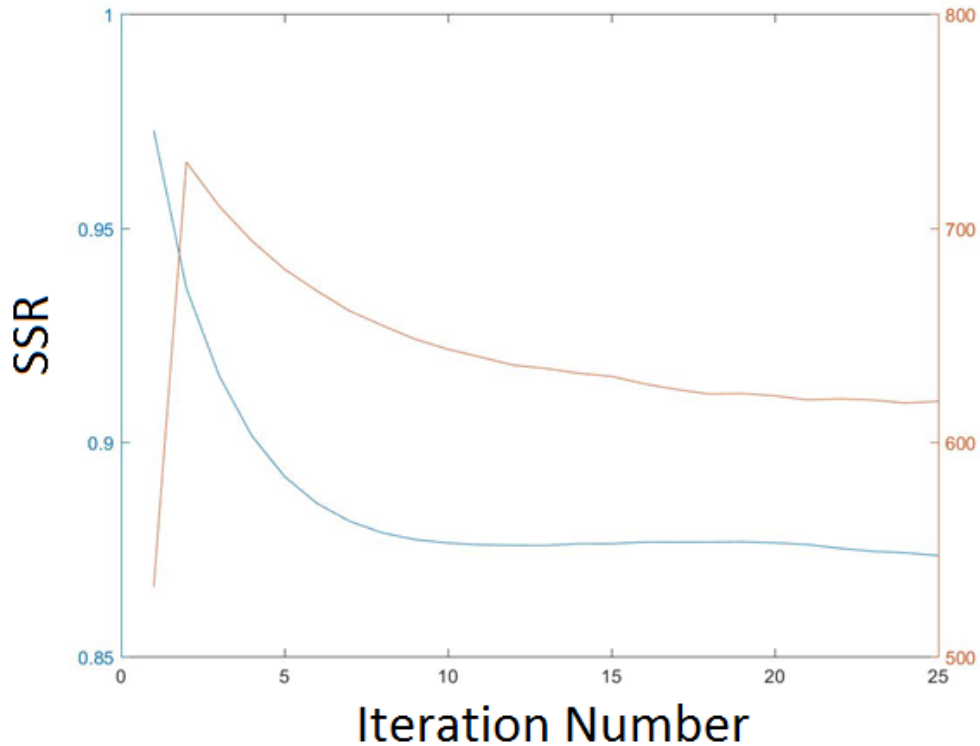


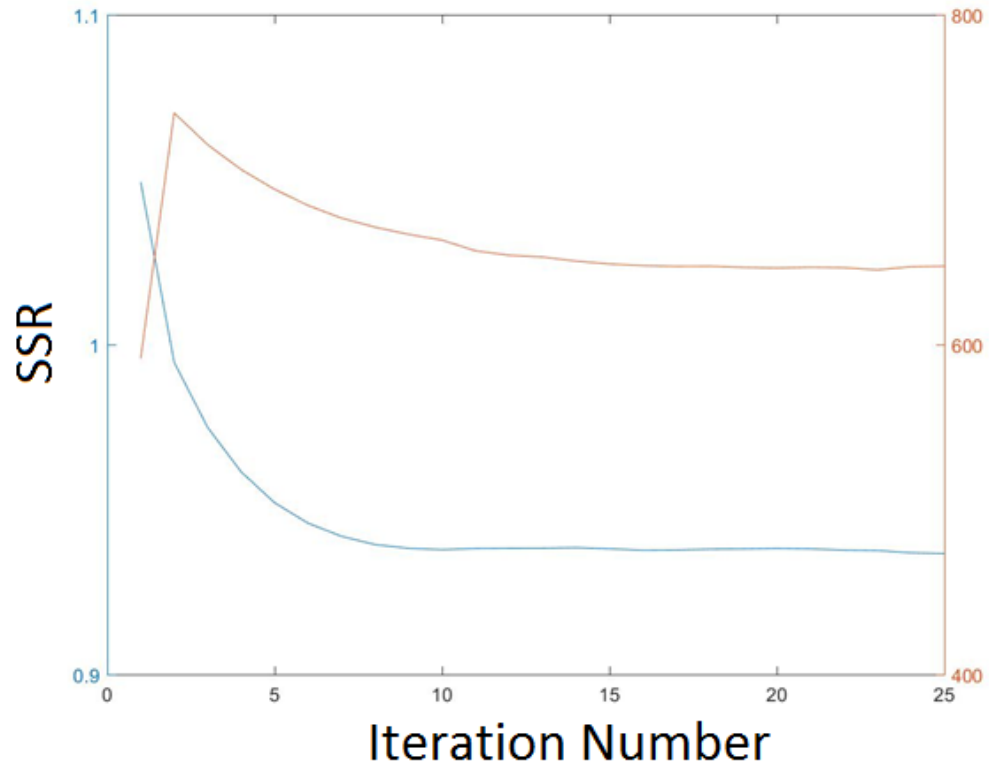
Figure A.1: Supporting tomograms for determining a grid size that fits the data set

Appendix B: Example SSR Curves

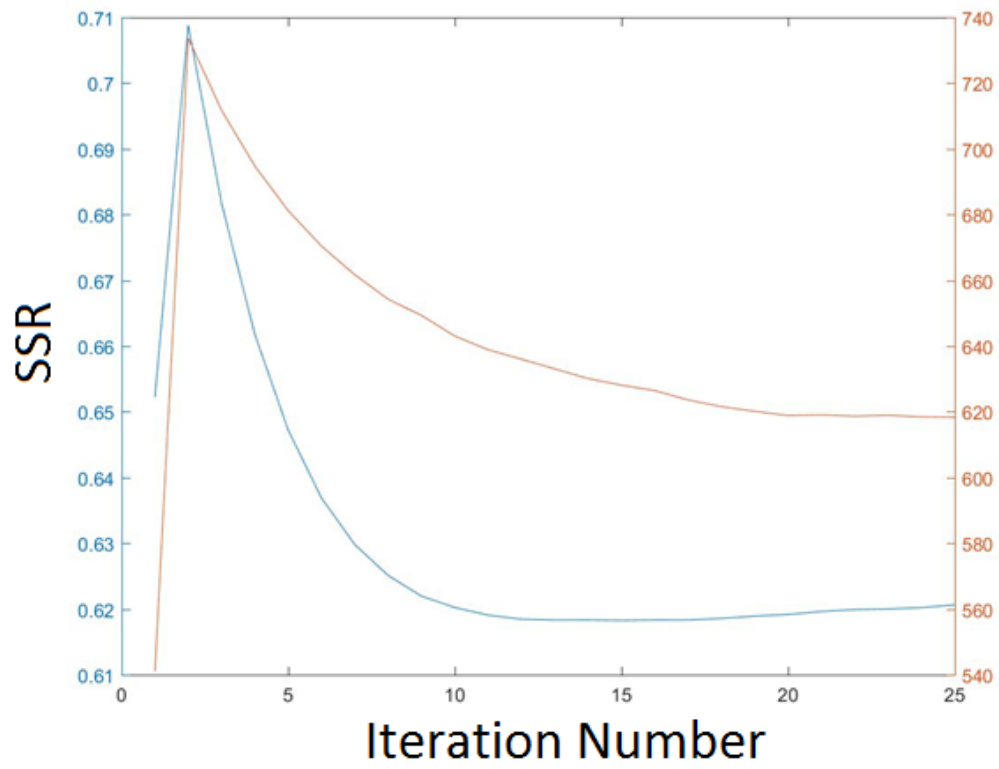
Appendix B shows examples of the SSR vs. iteration number curves used to pick the model that best fits the original travel time data. The first two examples are from the daily datasets and the final two are from the weekly datasets. The optimum iteration number is located at the elbow of the curve. Iteration numbers beyond this point tend to overfit the data and cause extreme values of high and low nodal velocity artifacts.



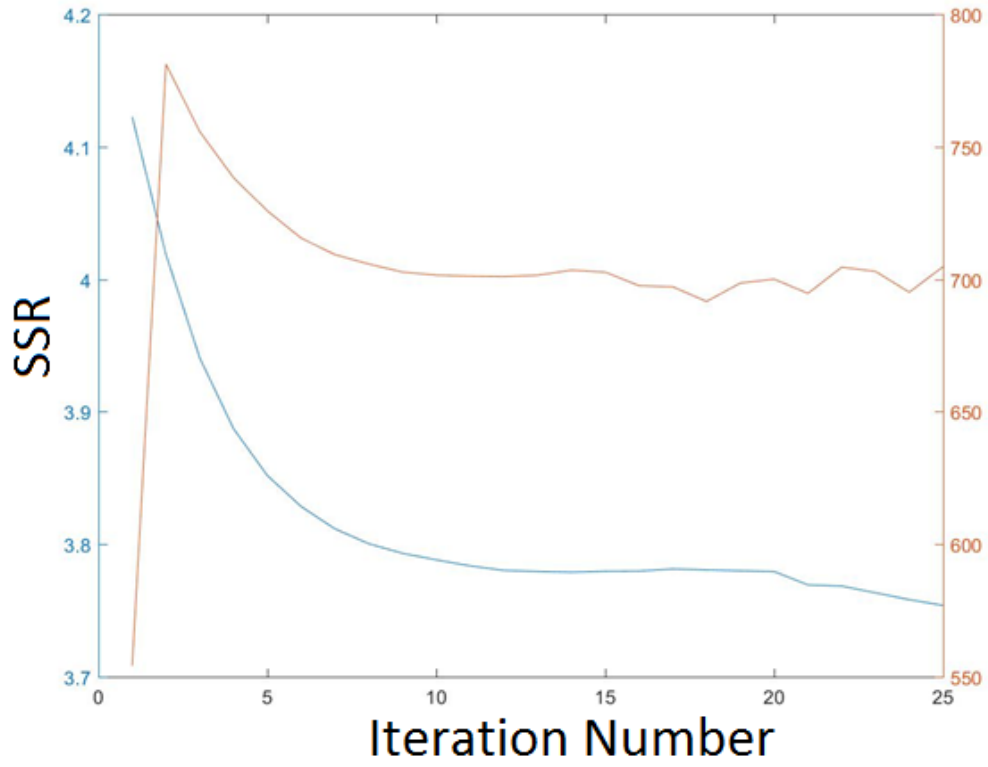
(a) March 1st – March 7th



(b) Mar. 6th – Mar. 12th



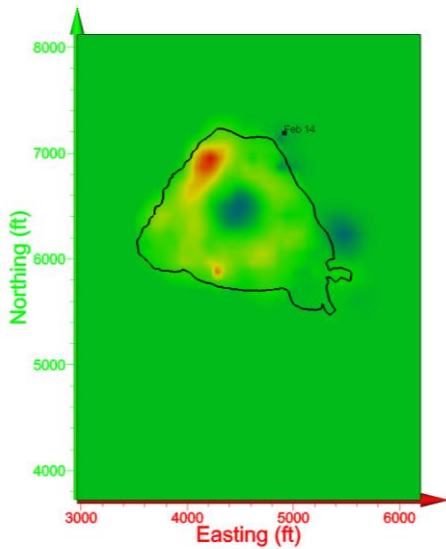
(c) Jan. 25th – Jan. 31st



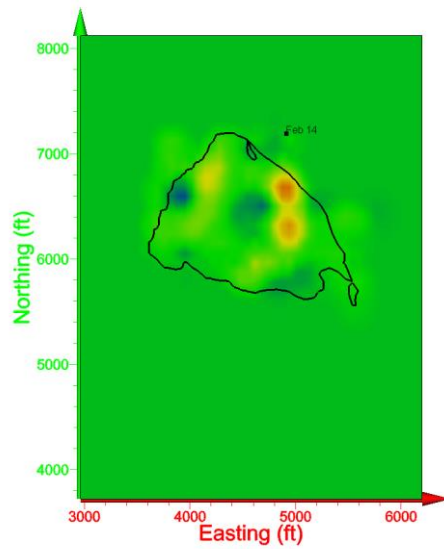
(d) Feb. 15th – Feb. 21st
Figure B.1: Example SSR vs. iteration number curves

Appendix C: Weekly Tomograms

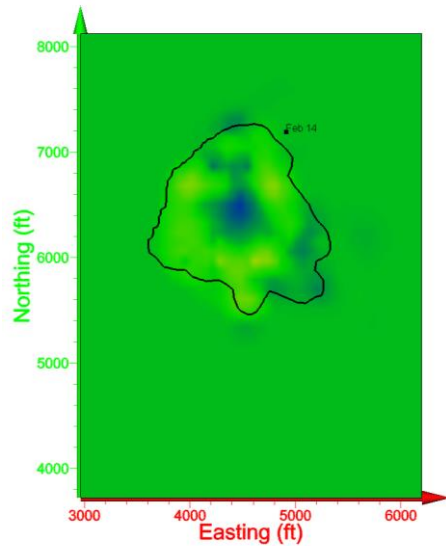
Appendix C includes cross sections of the tomograms that were calculated for the weekly datasets. Figure C.1 shows cross sections that were created on the axial plane at the depth of the February 14th event.



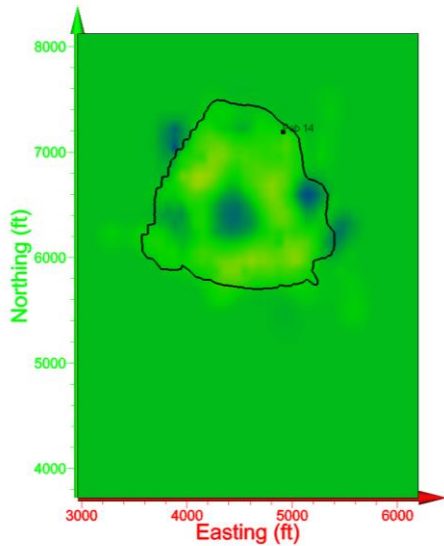
(a) Jan. 14th – Jan. 24th



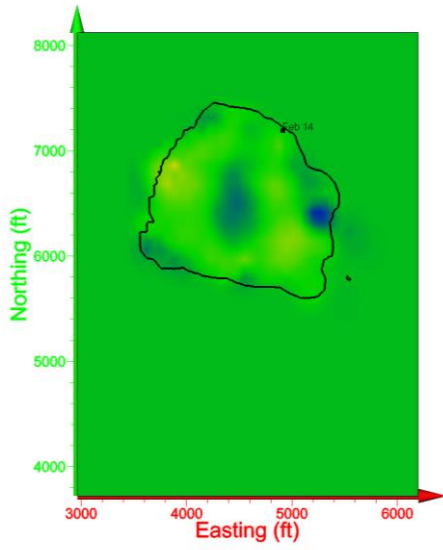
(b) Jan. 25th - Jan. 31st



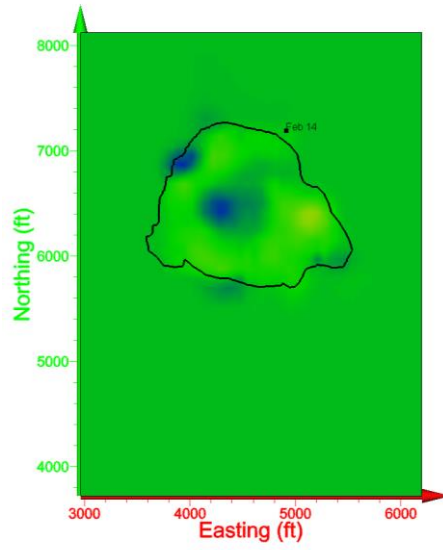
(c) Feb. 1st – Feb. 7th



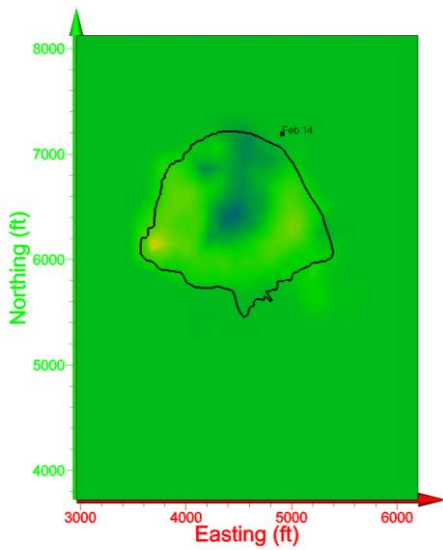
(d) Feb. 8th – Feb. 14th



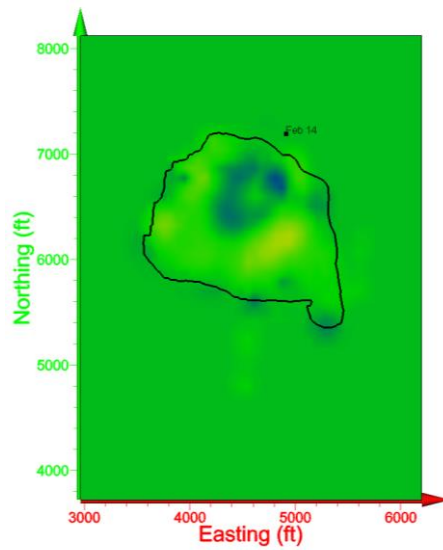
(e) Feb. 15th – Feb. 21st



(f) Feb. 22nd – Feb. 28th



(g) Mar. 1st – Mar. 7th



(h) Mar. 8th – Mar. 16th

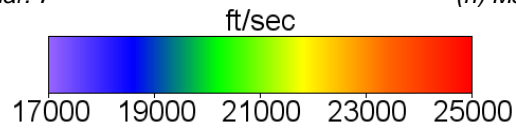
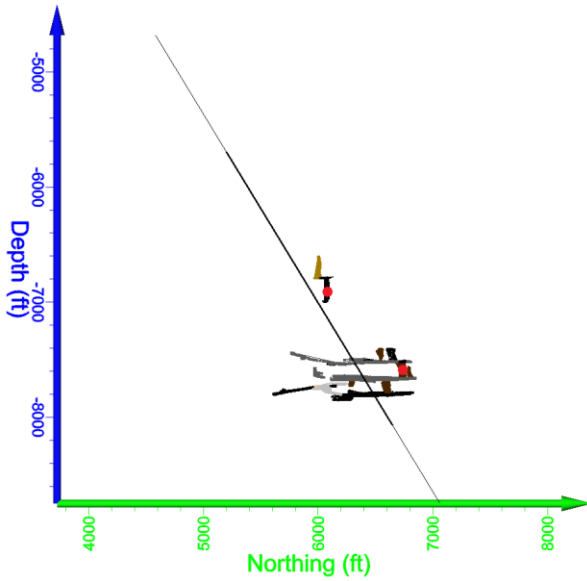


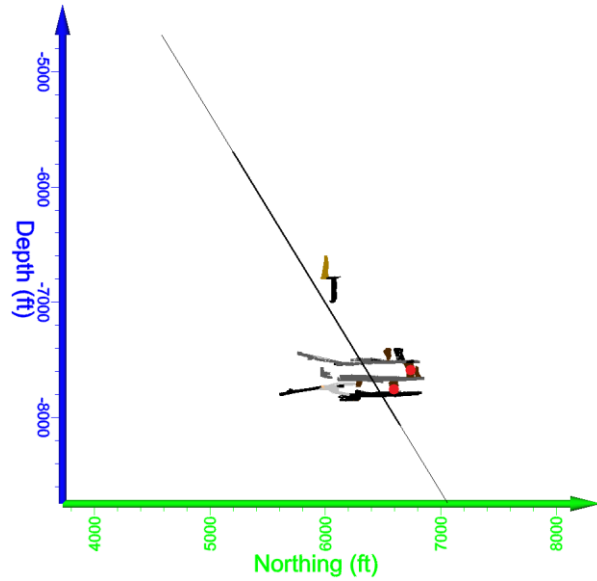
Figure C.1: Cross Sections on the axial plane at depth of February 14th event taken from weekly tomograms

Appendix D: Blast Locations

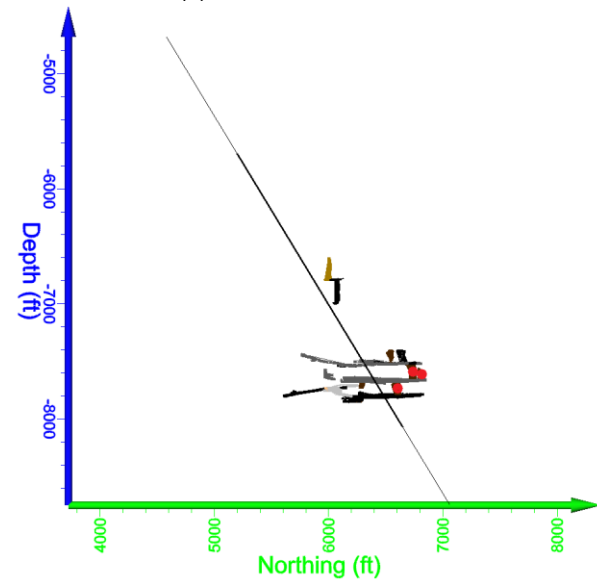
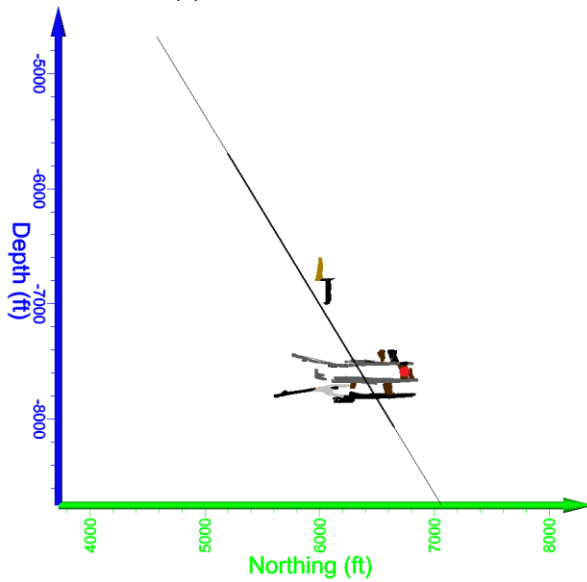
Appendix D includes plots of the blast locations that occurred during each of the weekly sets described in Table 3.1. Also noticeable in the plots is the oblique plane where a dense distribution of events occurred, including the March 14th event. The stopes that the blasts were conducted in are highlighted by red circles.



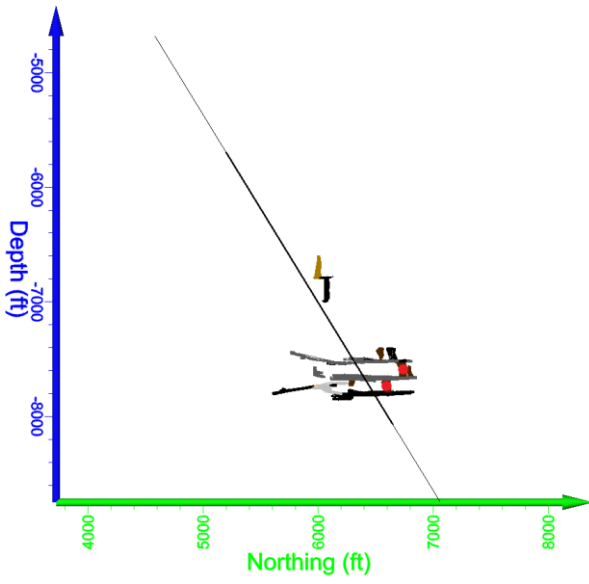
(a) Jan. 14th to Jan. 24th



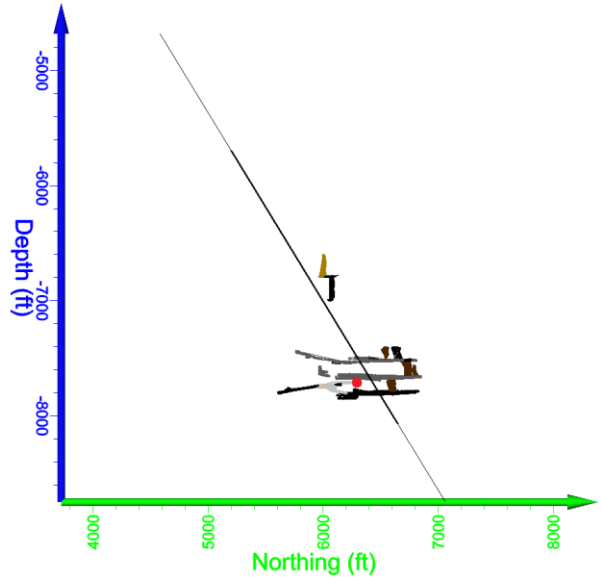
(b) Jan. 25th to Jan. 31st



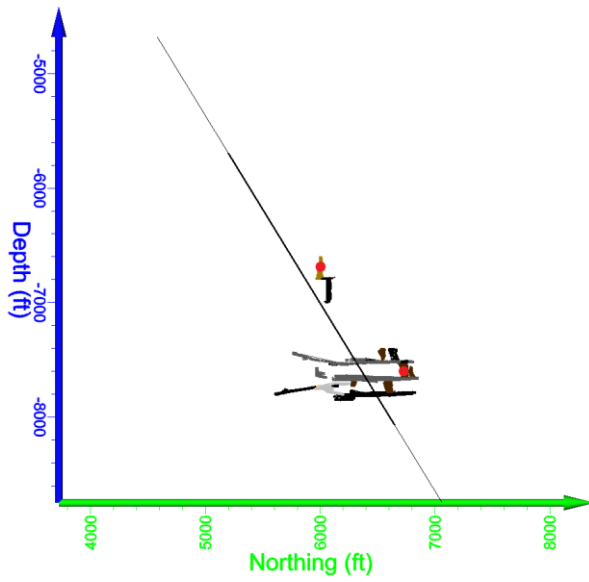
(c) Feb. 1st to Feb. 7th



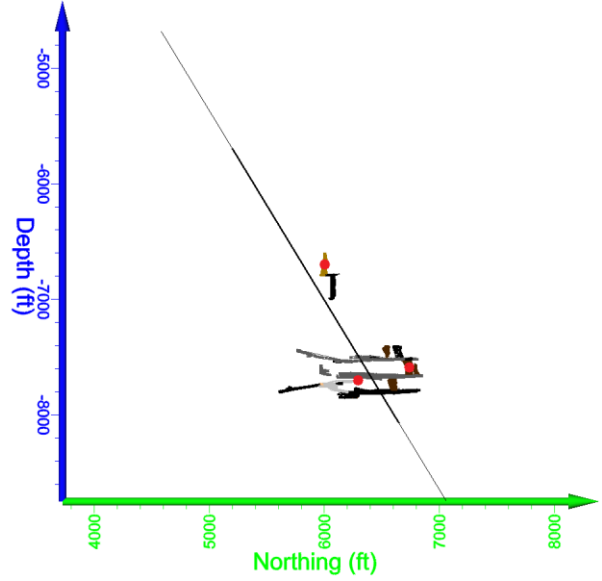
(d) Feb. 8th to Feb. 14th



(e) Feb. 15th to Feb. 21st



(f) Feb. 22nd to Feb. 28th



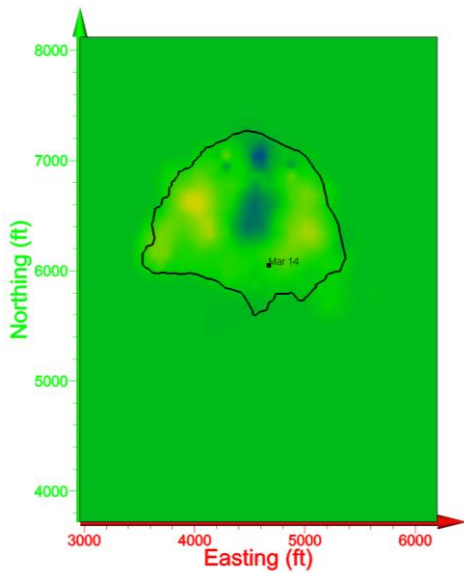
(g) Mar. 1st to Mar. 7th

(h) Mar. 8th to Mar. 16th

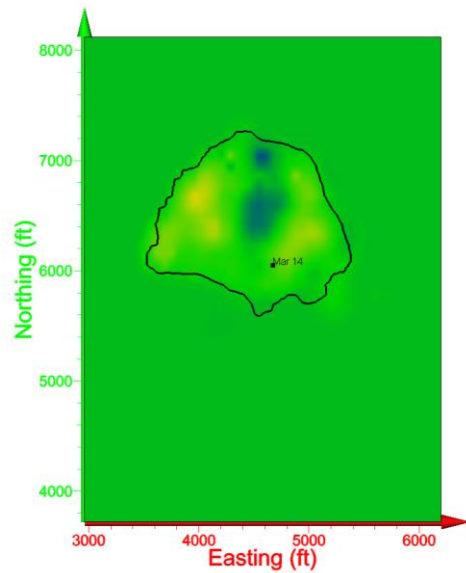
Figure D.1: Weekly blasting locations

Appendix E: Daily Tomograms

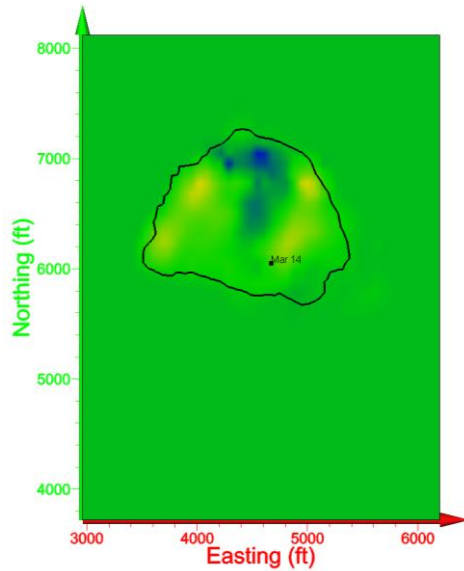
Appendix E includes supporting cross sections taken at various planes to show how the velocity field altered day-to-day. The cross sections were produced from tomograms that were calculated using the daily datasets. The cross sections shown in Figure E.1 were created on the axial plane at the depth of the March 14th event. Figure E.2 shows cross sections that were created on Plane A.



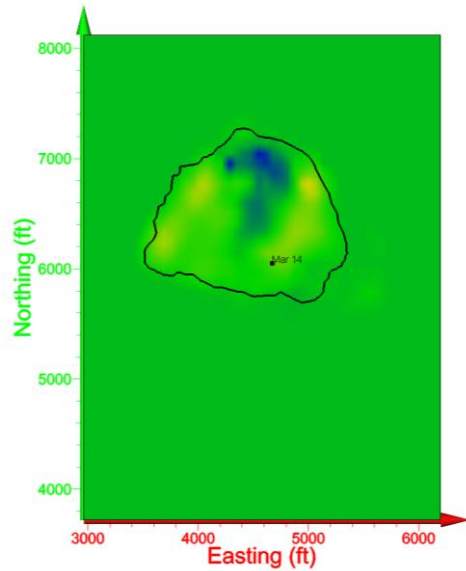
(a) Mar. 1st – Mar. 7th



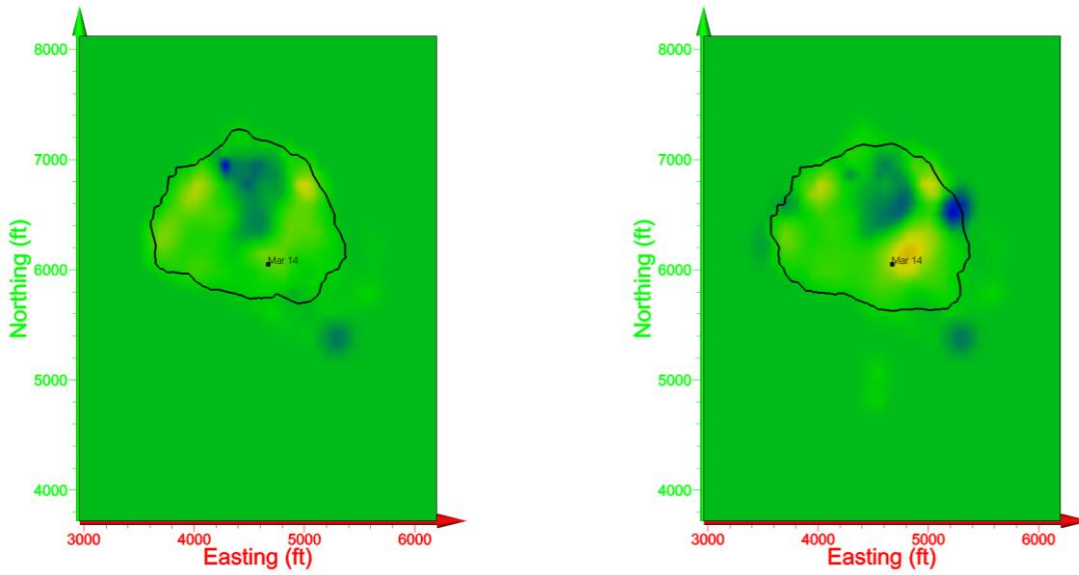
(b) Mar. 3^d – Mar. 9th



(c) Mar. 5th – Mar. 11th

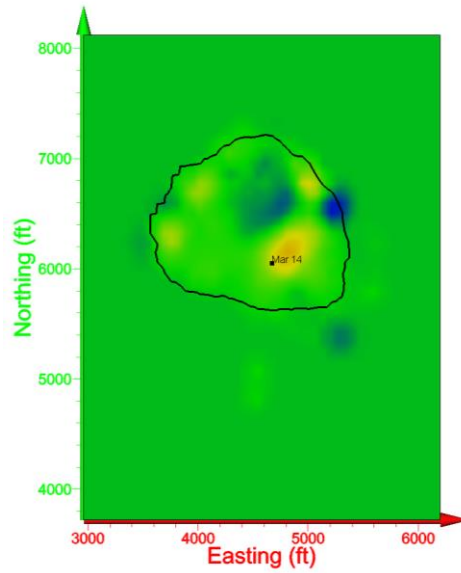


(d) Mar. 6th – Mar. 12th



(e) Mar. 7th – Mar. 13th

(f) Mar. 8th – Mar. 14th



(g) Mar. 9th – Mar. 15th

ft/sec

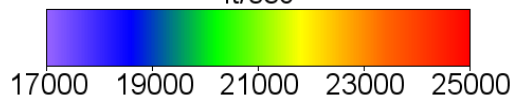
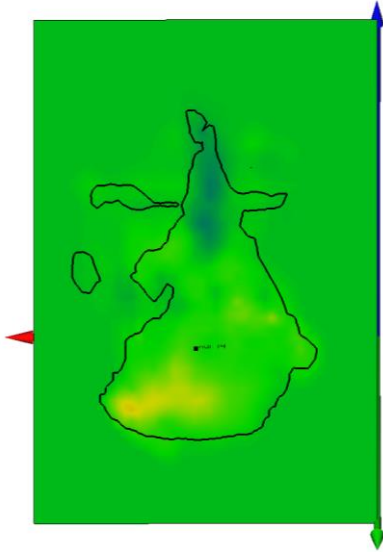
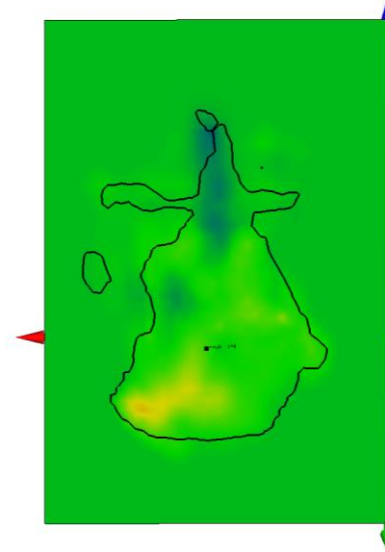


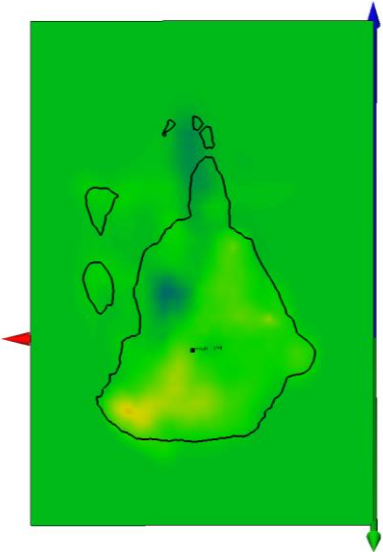
Figure E.1: Cross Sections on the axial plane at depth of March 14th event taken from daily tomograms



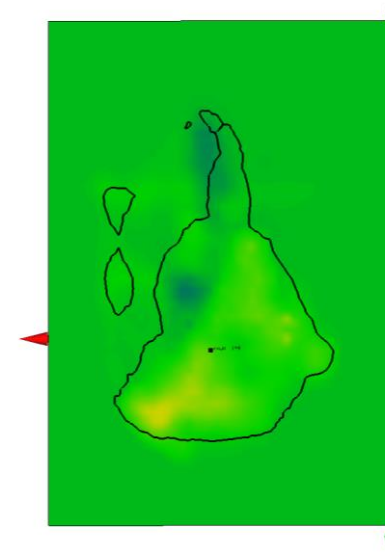
(a) Mar. 1st – Mar. 7th



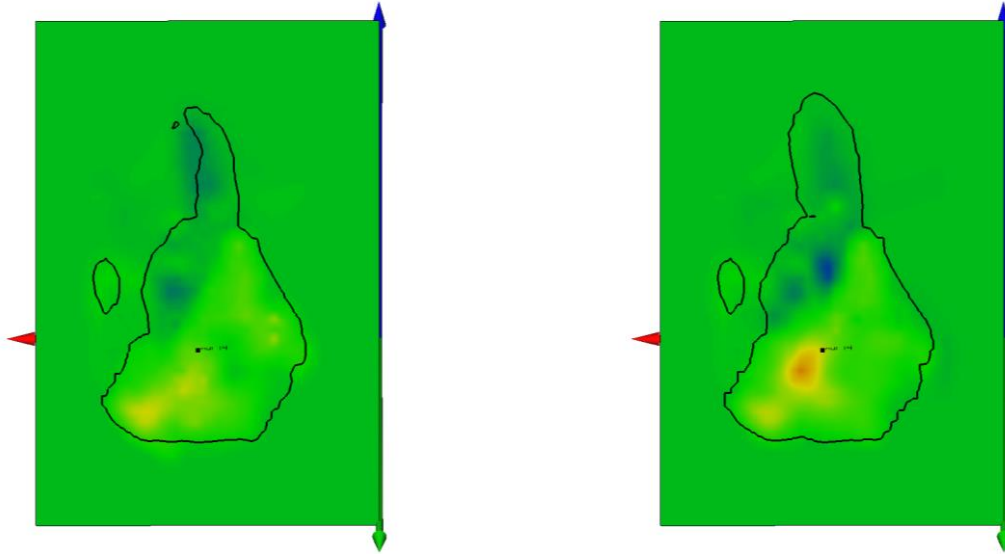
(b) Mar. 3rd – Mar. 9th



(c) Mar. 5th – Mar. 11th

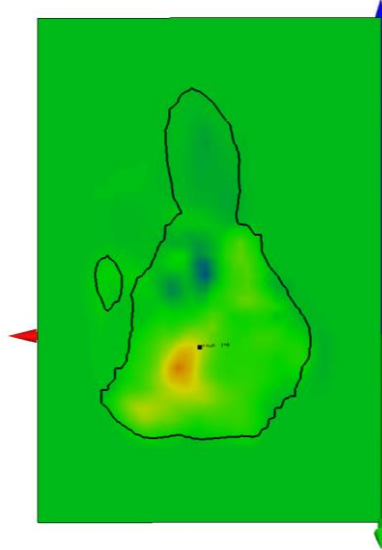


(d) Mar. 6th – Mar. 12th



(e) Mar. 7th – Mar. 13th

(f) Mar. 8th – Mar. 14th



(g) Mar. 9th – Mar. 15th
ft/sec

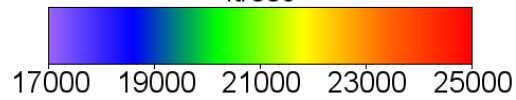


Figure E.2: Cross Sections on Plane A coincidental to the March 14th event taken from daily tomograms